2019

Hydrodynamic Modeling of Narragansett Bay in Support of the EcoGEM Ecological Model

David S. Ullman

Hydrodynamic Modeling of Narragansett Bay in Support of the EcoGEM Ecological Model

GSO Technical Report No. 2019-01

David S. Ullman, Christopher Kincaid, Christelle Balt, and Daniel L. Codiga

Graduate School of Oceanography
University of Rhode Island

January 24, 2019

Contents

List of Figures

List of Tables

1 Introduction

In response to the occurrence of persistent summertime hypoxia in Narragansett Bay (NB), the Coastal Hypoxia Research Program (CHRP) funded project "CHRP: Observations and Modeling of Narragansett Bay Hypoxia and its Response to Nutrient Management" focused on understanding how the interactions of physical and biological processes in NB result in hypoxic conditions. The ecological models used in this research were coarse-resolution box models where the entire NB area was subdivided into 15 boxes (Figure 2.1). Each box was further subdivided into an upper layer ($0 \geq z \geq -3.5$ m) and a lower layer (-3.5 m $\geq z \geq -H$, where H is the water depth), giving a total of 30 box model elements. The ecological model was of mid-level complexity with 6 state variables (for information on the ecological model see Vaudrey, 2016). The purpose of the hydrodynamic modeling was to provide realistic, time-varying inter-element mass exchanges for each state variable in the ecological model. This was performed using 1-day numerical dye tracer simulations for each day over a two-year period (2006-2007).

This report describes the hydrodynamic modeling of NB carried out in support of the NB-CHRP project. The hydrodynamic model, including the model configuration and forcing as well as model validation is detailed in Section 2. The parameterization of inter-element exchanges using dye tracers is described in Section 3.

2 Simulation of Narragansett Bay using the Regional Ocean Modeling System (ROMS)

2.1 Model Configuration and Forcing

The Regional Ocean Modeling System (ROMS) was adapted to NB using a nesting approach that allows for increased model spatial resolution in key areas (the upper portions of NB and the Providence River in this work). The high-resolution model domain, which was used to estimate property exchanges for EcoGEM, is shown in Figure 2.1. Spatial resolution was variable (Figure 2.2), with finest resolution in the Providence River (northern portion of the domain) where grid cell spacing was approximately 50 m in the east-west and 100 m in the north-south directions. As seen in Figure 2.1, the model spatial resolution was quite coarse (O(500 m)) in eastern Mount Hope Bay, an area that was not a focus of the CHRP project. The vertical discretization utilized a sigma coordinate system with 15 vertical levels. To reduce the size of the model grid, the Seekonk River, which extends northeast from the head of the Providence River, was replaced by a rectangular basin with the same surface area and volume as the real basin (see Figure 2.1). This ensures that tidal exchanges between the Seekonk and Providence Rivers are realistic although the circulation within the Seekonk (not a focus of the CHRP project) is not. Note that from the perspective of inter-element exchange in EcoGEM this should not be a major issue since the Seekonk is part of Box 1 (Figure 2.1) but is far from the boundary of the adjacent box (Box 2).

The high-resolution model domain was nested within a coarser resolution model domain, developed by Rogers (2008), that extended onto the continental shelf (Figure 2.3). The nesting was one-way, meaning that the output of the coarse-resolution model was used to force the high-resolution model but that the coarse-resolution model was not influenced by the high-resolution simulation. The same surface and river inflow forcing (described below) was used for both models.

2.1.1 Open Boundary Forcing. The coarse-resolution model was forced with surface elevation and depth-averaged velocity at the open boundaries (magenta points in Figure 2.3) using 9 tidal constituents (M_2, S_2, N_2, K_2, K_1, O_1, Q_1, M_4, M_6) from the Eastcoast tidal constituent database (Mukai et al., 2002) and, at subtidal timescales, with low-pass filtered output of the hindcast version of the Northeast Coastal Ocean Forecast System (NECOFS), a regional model covering the northeast U. S. coastal ocean (http://fvcom.smast.umassd.edu/necofs/). The surface elevation and depth-averaged velocity forcing was implemented in ROMS using the Chapman (1985) and Flather (1976) methodologies respectively. The depth-dependent velocity, temperature, and salinity in the coarse-resolution model were forced at the open boundaries using a combined radiation and nudging open boundary condition (Marchesiello et al., 2001) using low-pass filtered NECOFS output. The nudging timescales, τ_{nudge}, were varied depending on the direction of the depth-averaged current at the boundary,

with stronger nudging on inflow ($\tau_{nudge} = 1.6$h) than on outflow ($\tau_{nudge} = 24$h).

The output of the coarse-resolution model was extracted at the NB mouth and used to force the open boundary of the high-resolution model (green points in Figure 2.3). The same boundary forcing methodologies used for the coarse-resolution model were used for forcing the high-resolution model: surface elevation and depth-averaged velocity using the Chapman (1985) and Flather (1976) formulations and depth-dependent velocity, temperature and salinity using combined radiation and nudging (Marchesiello et al., 2001). The nudging time scales were shorter than were used for the coarse-resolution simulation in order to more tightly constrain the high-resolution model. The nudging time scales were $\tau_{nudge} = 1$h on outflow $\tau_{nudge} = 0.5$h on inflow.

2.1.2 Surface Flux Forcing. The models were also forced with surface heat and momentum fluxes estimated from meteorological variables obtained from models and local observations using bulk formulae (Fairall et al., 2003). All meteorological forcing except for 10 m height winds were assumed to be spatially uniform over the model domain. Spatially variable winds for the region were obtained from a data-assimilating, high resolution meteorological simulation of the northeast U.S. coastal region (Chen et al., 2005) which were provided by C. Chen at the University of Massachusetts. Air temperature and barometric pressure were estimated by averaging the measurements at the six stations of the Narragansett Bay PORTS system (http://www.co-ops.nos.noaa.gov/ports.html). Precipitation and relative humidity were obtained from observations at T. F. Green Airport, in Warwick RI. Net shortwave and downward longwave radiative fluxes were taken from the nearest gridpoint of NOAA's North American Regional Reanalysis model (http://www.emc.ncep.noaa.gov/mmb/rreanl). Upward longwave radiation was not specified, instead this quantity was computed based on the ocean surface temperature in the model simulations.

2.1.3 River Inflow Forcing. Freshwater discharge from local rivers and waste water treatment facilities (WWTF) was applied in the high-resolution model as point source inflows at the locations denoted by the red triangles in Figure 2.1. The rivers and/or WWTFs contributing to each source are given in Table 2.1. Most of the river point sources were implemented at a single ROMS gridpoint but, as indicated in Table 2.1, the discharge of two of the larger sources (rivers 2 and 3) was spread over 3 or 4 ROMS gridpoints to reduce the tendency for model instability.

Daily river discharge observations were obtained from the United States Geological Survey (USGS) for the eight rivers listed in Table 2.2. The gauging stations varied in their proximity to the locations at which the rivers discharge into NB. In order to account for the river discharge from the portion of the watershed downstream of the gauging station, the measured discharges were scaled up. The drainage areas upstream of each gauging station (available from USGS) were combined with estimates of the downstream drainage areas (provided by project collaborator M. Brush) to compute a drainage area ratio ($DAR = DA_{downstream}/DA_{upstream}$). The drainage area ratios are given in Table 2.2. The measured discharges for each river were corrected using these estimates, assuming that river discharge is proportional to drainage area using $Q_{corr} = Q_{meas} * (1 + DAR)$, where Q is discharge in m^3/s.

Freshwater discharges from the WWTFs, obtained from the operating organizations, did not need adjustment.

Freshwater discharge at two of the rivers listed in Table 2.1, Hardig Brook and the Maskerchugg River, were not regularly measured by the USGS. Initially, these very small river inflows were not included in the model, but evaluation of the model output suggested that the circulation and hydrography in Greenwich Bay was adversely affected by the lack of any freshwater entering the model domain at the west end of Greenwich Bay. As described further in the Appendix (Section 4.1), the discharges of these streams were estimated using a regression derived from historical measurements from the Maskerchugg and the nearby (gauged) Hunt River.

In addition to the gauged and ungauged rivers described above, there is additional ungauged drainage area bordering NB. In order to provide the best possible estimate of the total amount of freshwater discharged into NB, additional discharge associated with the ungauged drainage areas was computed, again assuming that discharge is proportional to drainage area. The total gauged drainage area (corrected for the ungauged portions of the gauged rivers) is 3735 km^2. The ungauged watersheds were divided into the part entering Mount Hope Bay (MHB) (229 km^2) and that entering the remainder of NB (347 km^2). The additional freshwater discharge into these subregions was computed from $Q_{add} = Q_{total} * DA_{add}/DA_{total}$, where Q_{add} and Q_{total} are the additional freshwater (to either MHB or NB) and the total gauged (corrected) freshwater inflows and DA_{add} and DA_{total} are the ungauged and total gauged drainage areas given above. Finally, the additional discharge amounts (15% of the total gauged discharge) are partitioned as follows: (a). the MHB additional discharge is added to the Taunton River and (b). the NB additional discharge is distributed evenly among the Pawtuxet, Palmer, and Hunt Rivers.

River forcing in ROMS requires, in addition to the river discharge discussed above, specification of the vertical profile of the river inflow transport and the concentration of tracers in the inflowing water. The vertical profile of the river inflow was specified as vertically uniform. Salinity of the inflowing water was set to 0. Time varying river water temperature was estimated using a regression equation involving air temperature as well as water temperature on the previous day (see Section 4.2 for details of this computation). Each river inflow source was marked with a unique numerical dye tracer with a concentration of 1 kg/m^3 in the inflowing water. Concentrations of all other numerical dyes (marking all other rivers and all box model elements, as will be described below) were set to zero in the river inflows.

2.1.4 Model Parameterizations. Vertical mixing of momentum and tracers in the model was parameterized using an eddy viscosity/diffusivity formulation. The temporally and spatially variable eddy viscosity and diffusivity were computed using the results of an embedded two-equation turbulence model and empirical functions of water column stability. Of the several available turbulence closure models, we used the $\kappa - \epsilon$ model (e.g. Warner et al., 2005), which solves prognostic equations for the turbulence kinetic energy (κ) and the dissipation rate of turbulence kinetic energy (ϵ). The ROMS default stability functions, from Galperin et al. (1988), were used in the computation of the eddy viscosity and diffusivity from the modeled κ and ϵ. Model

ROMS River	Sources Included	River Points
1	Moshassuck, Woonasquatucket	1
2	Blackstone, Ten Mile, Bucklin Point*	4
3	Pawtuxet	3
4	Taunton	1
5	Hunt	1
6	Palmer	1
7	Fields Point*, E. Providence*	1
8	Hardig Brook	1
9	Maskerchugg, E. Greenwich*	1

Table 2.1: Freshwater inflow information for the high-resolution NB ROMS model. The ROMS river number refers to the numbered locations in Figure 2.1. Sources marked with an asterisk are WWTFs. The last column indicates the number of ROMS gridpoints at which river inflow is applied (if greater than 1, the discharge is distributed equally over this number of gridpoints).

.

runs using several of the other turbulence closure schemes available in ROMS showed that the results were insensitive to the specific choice of the closure model, with all of the two-equation models tested producing similar model skills (Balt, 2014).

Bottom stress in the model was computed under the assumption that the near-bottom velocity profile is logarithmic and that within this logarithmic layer the velocity does not vary in direction. The kinematic bottom stress components (τ_{bx} and τ_{by}) are computed using a quadratic formulation:

$$\tau_{bx} = C_D u_b \sqrt{u_b^2 + v_b^2} \tag{2.1}$$

$$\tau_{by} = C_D v_b \sqrt{u_b^2 + v_b^2}, \tag{2.2}$$

where u_b and v_b are the x and y velocity components at the near-bottom sigma level and C_D is the drag coefficient. The assumption that the velocity profile is logarithmic allows the drag coefficient to be expressed in terms of the bottom roughness length as:

$$C_D = \frac{\kappa^2}{[\ln(z_b/z_0)]^2}, \tag{2.3}$$

where $\kappa = 0.41$ is von Karman's constant, z_b is the height above the bottom of the lowest sigma level, and z_0 is the bottom roughness. Lacking sufficient information as to the spatial variability of bottom type within the Bay, the model bottom roughness length was set to a constant value: $z_0 = 0.001$ m.

Sub-gridscale horizontal mixing of momentum and tracers was parameterized using a Laplacian formulation with scale-dependent viscosity and diffusivity. The maximum horizontal viscosity and diffusivity were set to 2 m^2/s. These values were scaled by the ratio of the local grid spacing to the maximum grid spacing to produce spatially variable fields, where the minimum values were ~ 0.2 m^2/s.
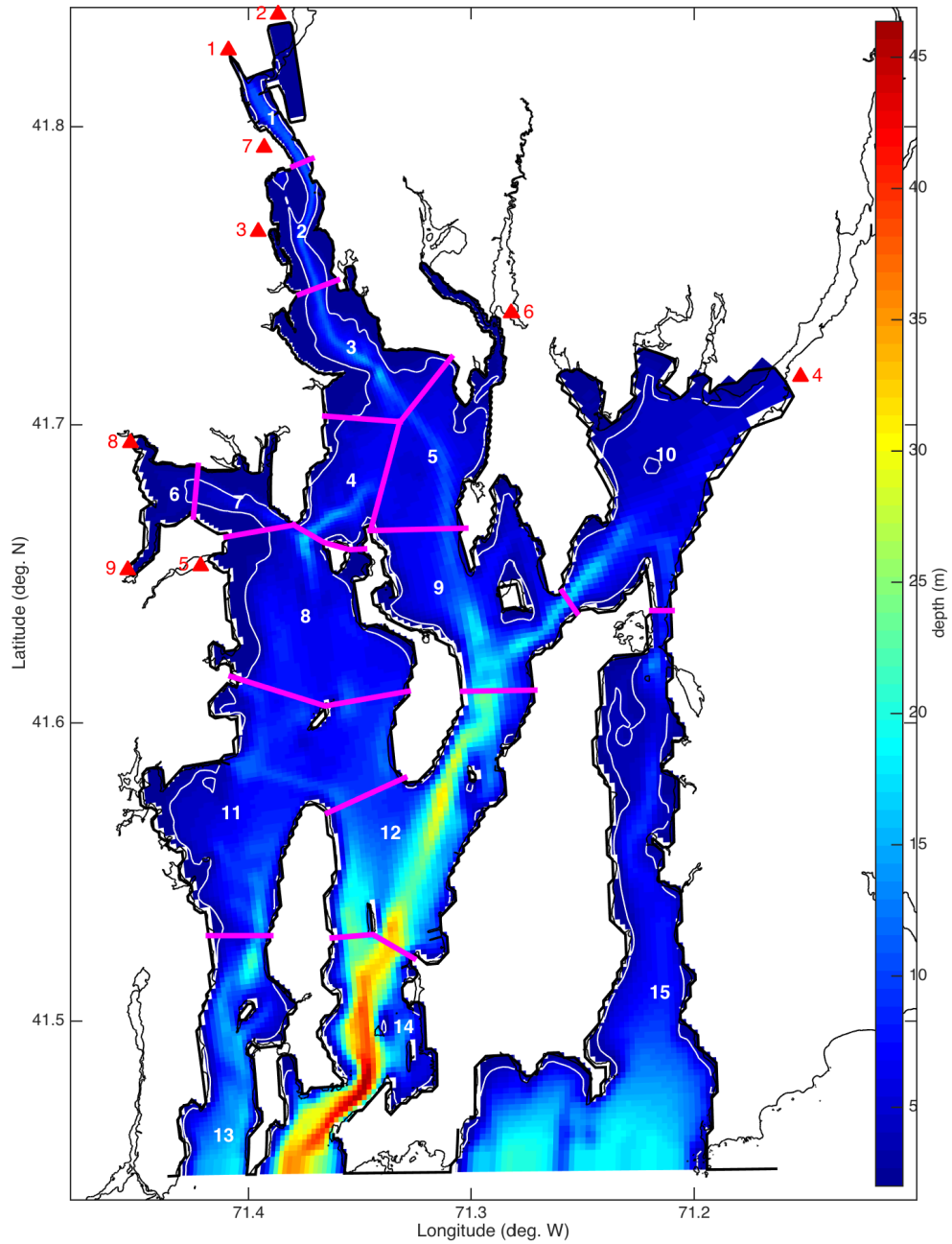
Figure 2.1: Bathymetry of the Narragansett Bay fullbay model domain showing the horizontal boundaries of the EcoGEM box model elements (magenta lines). The colored region indicates the water portion of the model domain (colored proportional to water depth) and the light black line shows the actual coastline. The white numbers indicate the EcoGEM box number. The locations of freshwater inflow are indicated by the red triangles. The red numbers refer to the river identification numbers in Table 2.1.

River	USGS Site Number	Drainage Area Ratio
Woonasquatucket @ Centerdale	01114500	0.32
Moshassuck @ Providence	01114000	0.02
Blackstone @ Woonsocket	01112500	0.14
Ten Mile @ E. Providence	01109403	0.04
Pawtuxet @ Cranston	01116500	0.16
Taunton @ Bridgewater	01108000	1.05
Palmer @ South Rehoboth	01109220	0.57
Hunt @ East Greenwich	01117000	0.00

Table 2.2: Ratio of ungauged drainage to gauged drainage area for the rivers entering Narragansett Bay for which USGS discharge measurements are available.
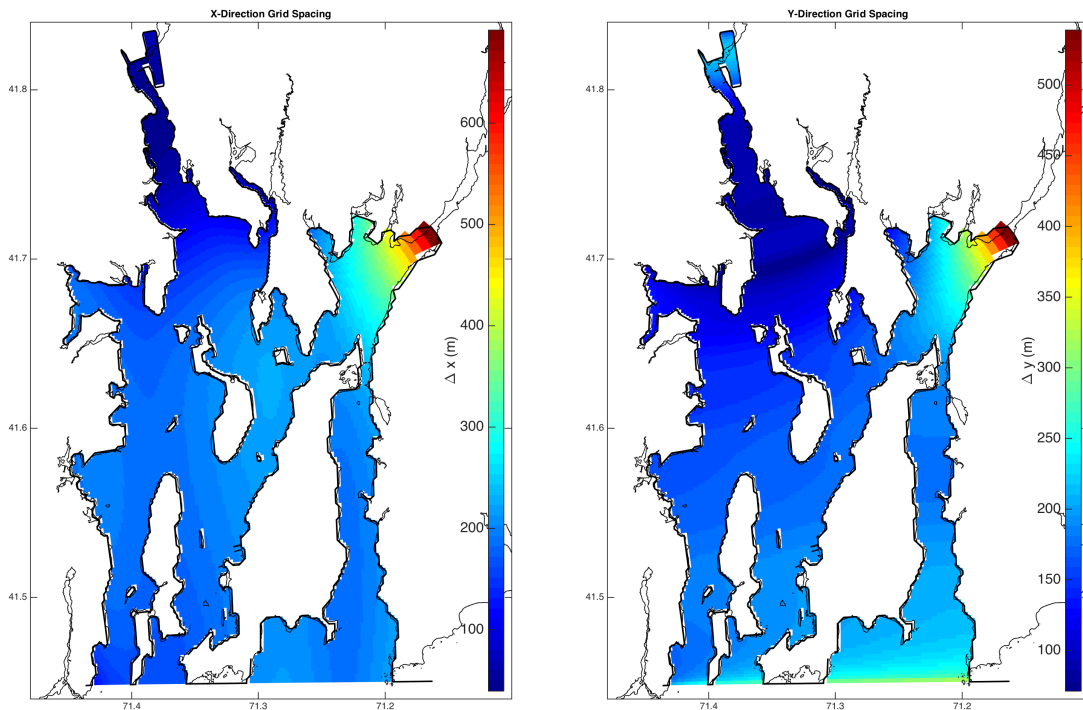
(a) X-direction spacing (m)

(b) Y-direction spacing (m)

Figure 2.2: Model grid spacing in x (roughly east-west) and y (roughly north-south).
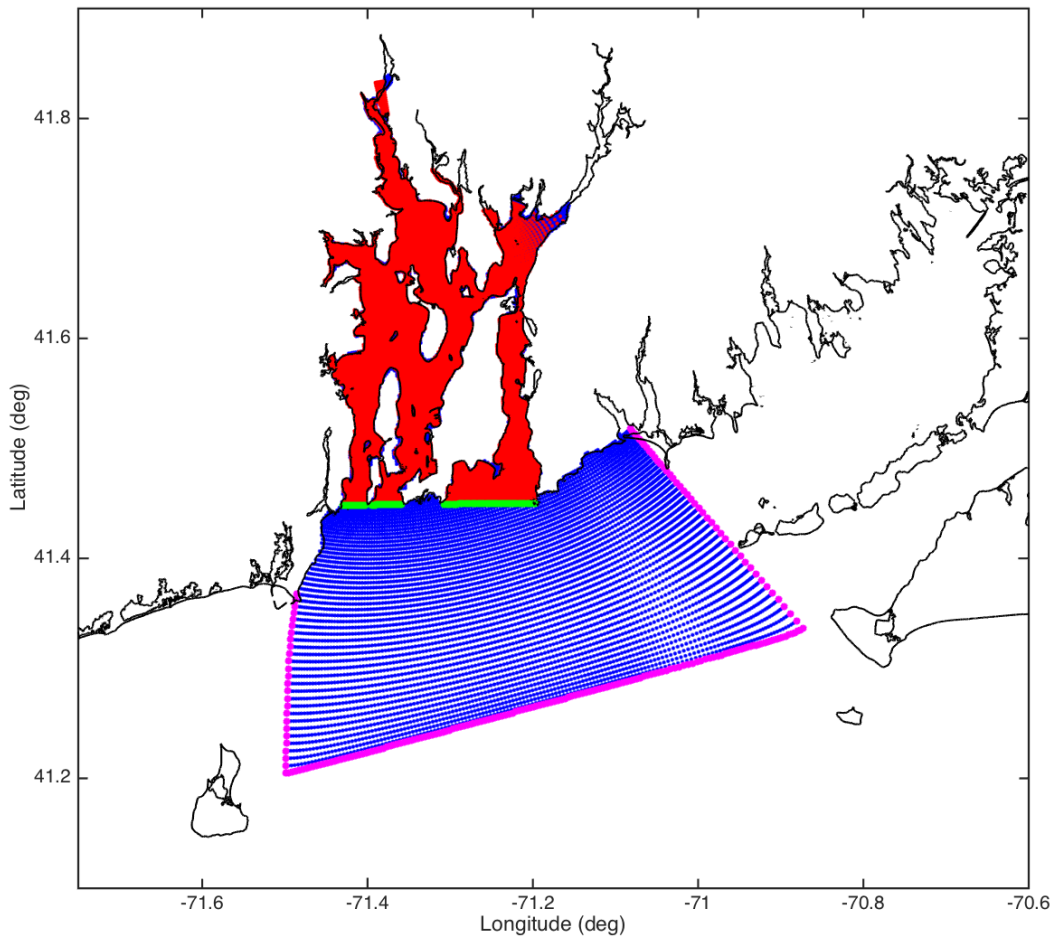
Figure 2.3: Nested ROMS model grids. The blue points are the gridpoints for the low-resolution model extending onto the continental shelf. The magenta points show the locations where the low-resolution model is forced by tides and the output of a regional circulation model. The red points are the gridpoints of the high-resolution model of NB. The green points show the locations where output of the low-resolution model is used to force the high-resolution model.

2.2 Model Validation

To ensure that the high-resolution ROMS model would provide realistic mass exchanges for the EcoGEM model, the ROMS output was validated extensively against observations in NB. The observations included water surface elevation from local tide gauges, currents from bottom-mounted acoustic Doppler current profilers (ADCPs), and temperature and salinity from the network of fixed site monitoring stations in the middle and upper bay. The development of the NB nested modeling system was an iterative process. For example, an initial version did not make use of regional model output (NECOFS) for open boundary forcing of the coarse-resolution model, nor did it include spatially variable wind forcing or rivers entering Greenwich Bay. The addition of each of these components improved model fidelity (compared to the observations) at least somewhat. In what follows, in order to simplify the presentation, we present comparisons of model output and observations only for the final version of the model (details of which are described in Section 2.1).

Several different measures of model fidelity to observations is presented in this section. These include time series comparison plots, Taylor diagrams (Taylor, 2001), and model skill estimates (Willmott, 1982). The latter two techniques will now be briefly described. The interested reader can consult the cited references for further information.

The Taylor diagram (Taylor, 2001) combines several statistical measures of a model variable and the associated observations into a single diagram. These are (1) the correlation coefficient and (2) the root-mean-square (rms) difference between the model variable and its observational counterpart, and (3) the standard deviation of the model variable. The mean values of both the model and observational variables are subtracted prior to computing these statistics. In order to allow for the evaluation of multiple model variables (or the same variable at different locations) on the same diagram, the rms difference and the model standard deviation are normalized (divided) by the standard deviation of the observational variable. Figure 2.9 shows an example of a Taylor diagram, where a particular model-observation comparison is represented by a single point. The radial position of the point gives the normalized standard deviation of the model variable, the azimuthal position gives the model-observation correlation, and the normalized rms difference is given by the position of the point relative to the gray concentric dashed circles whose center lies along the horizontal axis at the red point. This location, where the normalized standard deviation is 1 (standard deviation of the model equals that of the observations), the correlation is 1, and the normalized rms difference is zero represents a perfect model that exactly replicates the observations. The fidelity of the model simulation of a given variable is given by the distance of the model point relative to this reference point.

The use of the skill metric to evaluate a model is driven by the desire to represent model performance by a single number. Several different model skill definitions can be found in the literature, but in this report the skill metric of Willmott (1982) is

used. The Willmott skill is defined as:

$$Skill = 1 - \frac{\sum_{i=1}^{N}(x_i^{mod} - x_i^{obs})^2}{\sum_{i=1}^{N}(|x_i^{mod} - \overline{x^{obs}}| + |x_i^{obs} - \overline{x^{obs}}|)^2}, \tag{2.4}$$

where x_i^{mod} and x_i^{obs} are the ith model and observational values, the overbars represent time mean values, and the summations are over N pairs of values. A skill value of one indicates a model that perfectly replicates the observations, while a value of zero indicates that the model has no skill in simulating them.

2.2.1 Surface elevation. Hourly water surface elevation measurements were obtained from tide gauges operated by the National Ocean Service (NOS) at Newport, Quonset Point, Conimicut Light, and Providence (see Figure 2.4). At each station, the mean water elevation was subtracted from the observations in order to reference the measurements to local mean sea level (over the 2-year model period) which is the nominal model reference. Surface elevations from the high-resolution model, interpolated by ROMS to the tide gauge locations, were output every 2 hours and were subsequently interpolated to the observation times to facilitate comparison.

The comparison of model and observed surface elevation is performed in two frequency bands, tidal frequencies ($f > 1/36\,\mathrm{h}^{-1}$) and subtidal frequencies ($f < 1/36\,\mathrm{h}^{-1}$). The raw observations and model output were low-pass filtered, with a 36 h filter cutoff period, to produce subtidal time series. The subtraction of the low-pass filtered series from the raw time series provides the tidal time series. Visual comparison of the model and observed surface elevation at the four NOS sites and separated into subtidal and tidal bands is shown in Figures 2.5–2.8. These figures indicate the general agreement of the model tidal (bottom panels) and subtidal fluctuations (top panels) with the observations at all sites. Tidal amplitudes are slightly underpredicted in the model but the spring-neap variability is well simulated. Subtidal fluctuations appear to be somewhat less well captured by the model although the level of variability and the seasonal cycle both agree well with the observations.

A more quantitative view of the model surface elevation simulation in the two frequency bands is shown by the Taylor diagrams (Taylor, 2001) in Figure 2.9. In the tidal band (Figure 2.9 bottom), the model normalized standard deviation is approximately 0.8, indicating that tidal fluctuations are underpredicted by about 20%. Because the normalized standard deviation is nearly the same at all sites, suggesting that the tide is not being abnormally damped as it propagates up the bay, it appears that the tidal underprediction may result from inadequate tidal forcing at the model open boundary. At tidal frequencies, the correlation coefficient between model and observations is ≥ 0.95 at all sites. Normalized rms differences between observations and model surface elevations are approximately 0.25, meaning that rms differences are 25% of the observation standard deviations. The observation standard deviations, shown in Table 2.3, at tidal frequencies are approximately 0.40 m, thus the rms model-observation differences are about 0.1 m. Model skills in the tidal band are all above 0.97 (Table 2.3), again indicating that tides are well simulated by the model.

At subtidal frequencies (Figure 2.9 top), the model produces the correct level of variability as indicated by the normalized standard deviation value of 1. The

16

Station	σ_{tidal} (m)	σ_{subtidal} (m)	Skill$_{\text{tidal}}$	Skill$_{\text{subtidal}}$
Newport	0.38	0.13	0.98	0.84
Quonset	0.40	0.13	0.98	0.82
Conimicut	0.43	0.13	0.97	0.84
Providence	0.45	0.14	0.97	0.85

Table 2.3: Water level standard deviations (σ) and model skill at tidal and subtidal timescales for each tide gauge station.

correlation between model and observations is lower than at tidal frequencies, however the correlation values of $0.65 - 0.75$ nonetheless indicate substantial model predictive capability. The normalized rms differences at subtidal frequencies are of the order of $0.75 - 0.80$ or $75 - 80\%$ of the observation standard deviations. From Table 2.3, the subtidal observational standard deviations are about 0.13 m, thus the rms model-observation differences in this frequency band are approximately 0.1 m. Model skills in the subtidal band are in the range $0.82 - 0.85$ (Table 2.3), indicating that subtidal fluctuations are reasonably well simulated by the model.
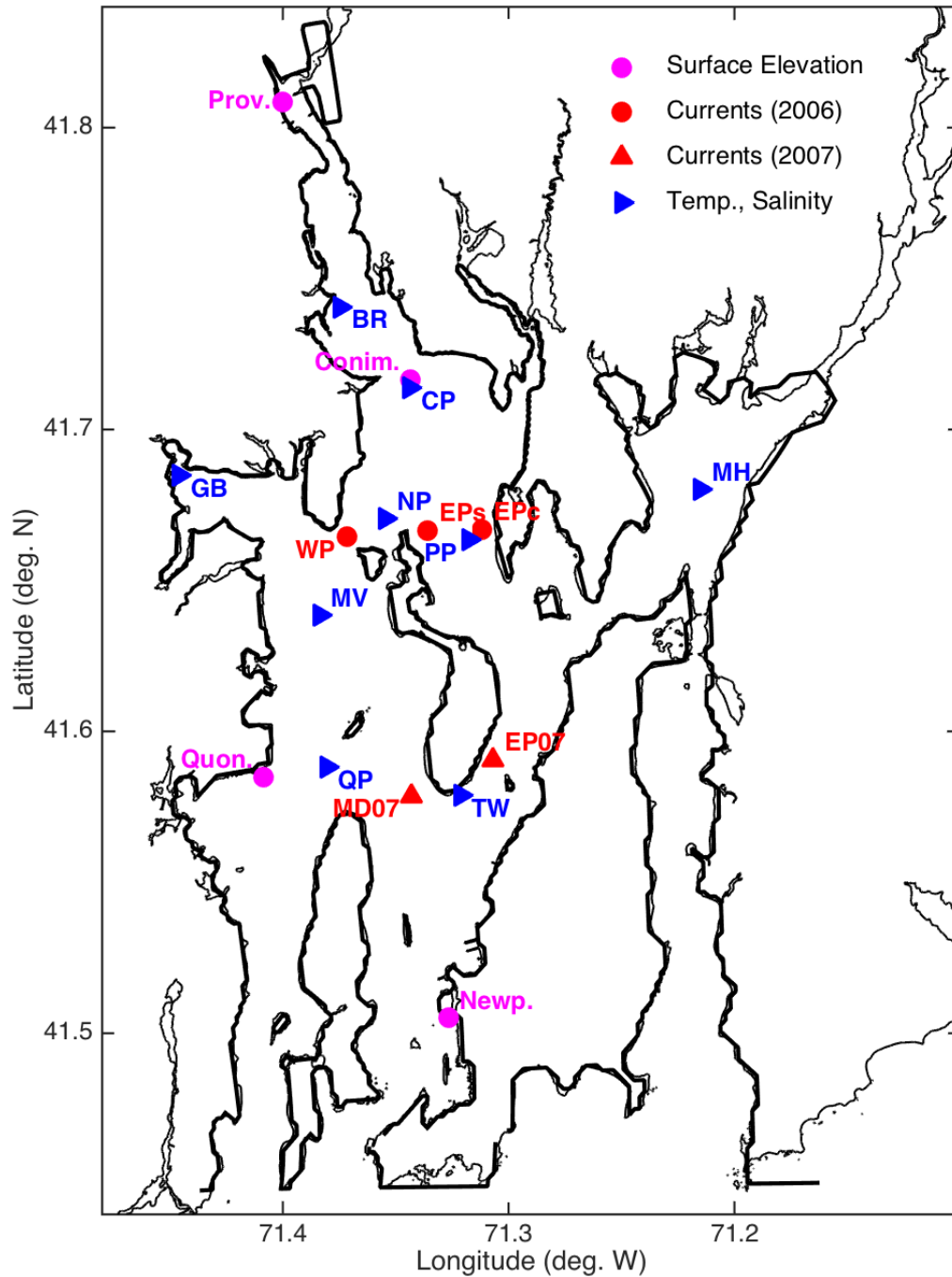
Figure 2.4: Map showing locations of surface elevation (magenta symbols), currents (red), and temperature/salinity (blue) observations used for model validation. The light and heavy dark lines are the actual coastline and the high-resolution model coastline respectively.
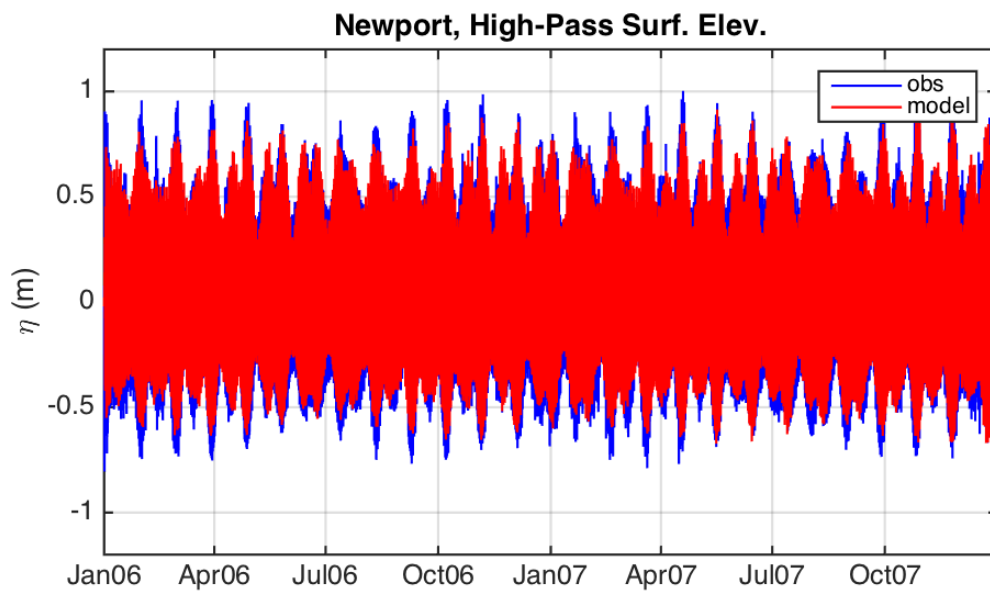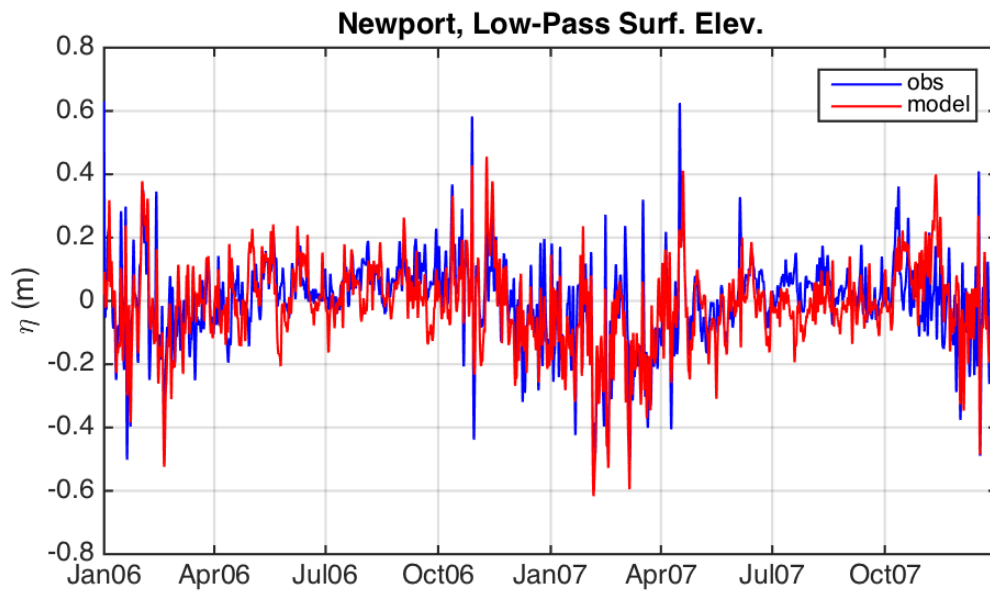
Figure 2.5: Comparison of surface elevation at Newport from model and observations. The time series are separated into (top) subtidal (low-pass filtered) and (bottom) tidal (hgh-pass filtered) frequency bands.
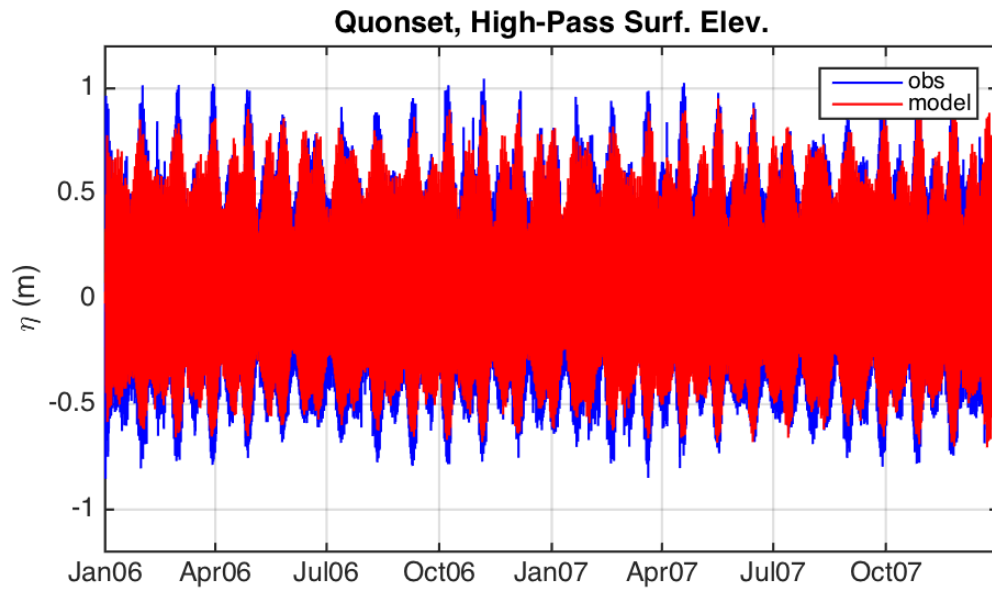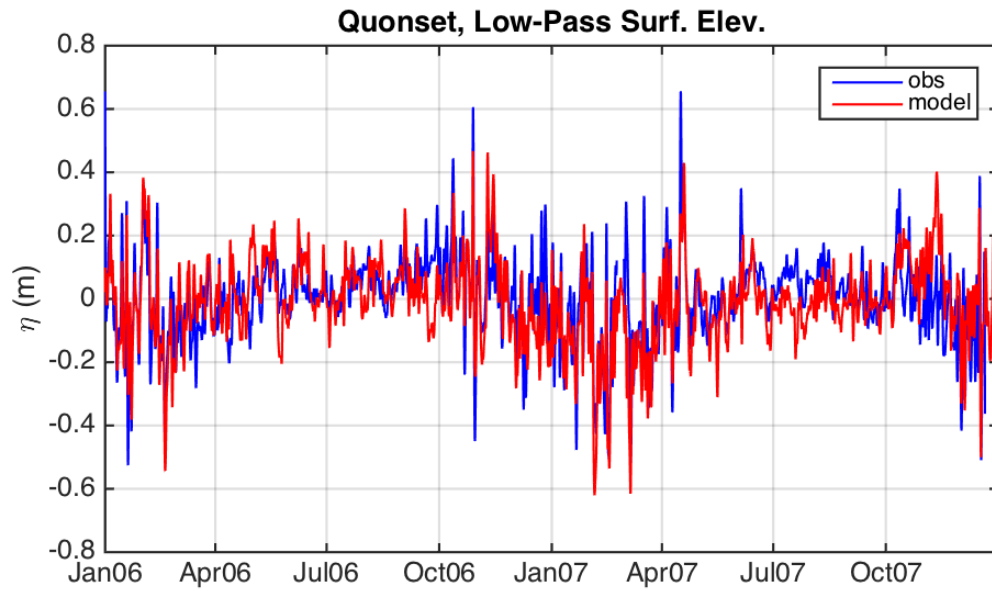
Figure 2.6: Comparison of surface elevation at Quonset Point from model and observations. The time series are separated into (top) subtidal (low-pass filtered) and (bottom) tidal (hgh-pass filtered) frequency bands.
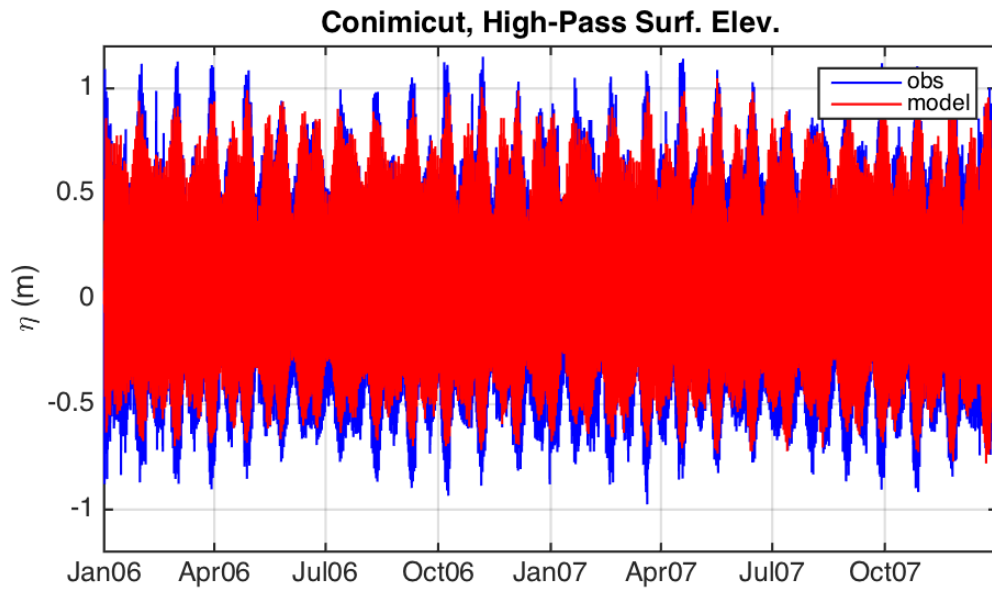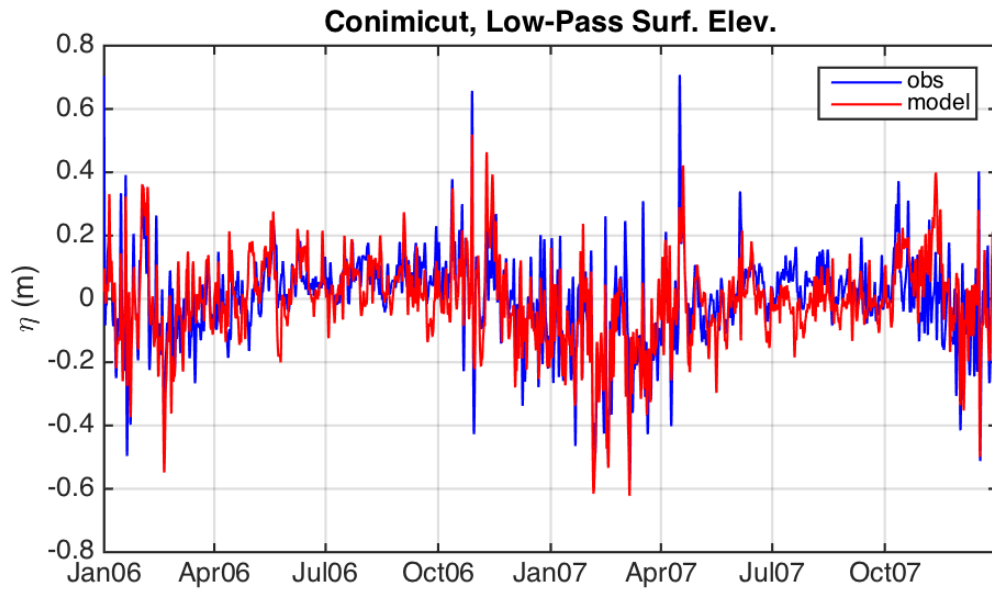
Figure 2.7: Comparison of surface elevation at Conimicut from model and observations. The time series are separated into (top) subtidal (low-pass filtered) and (bottom) tidal (hgh-pass filtered) frequency bands.
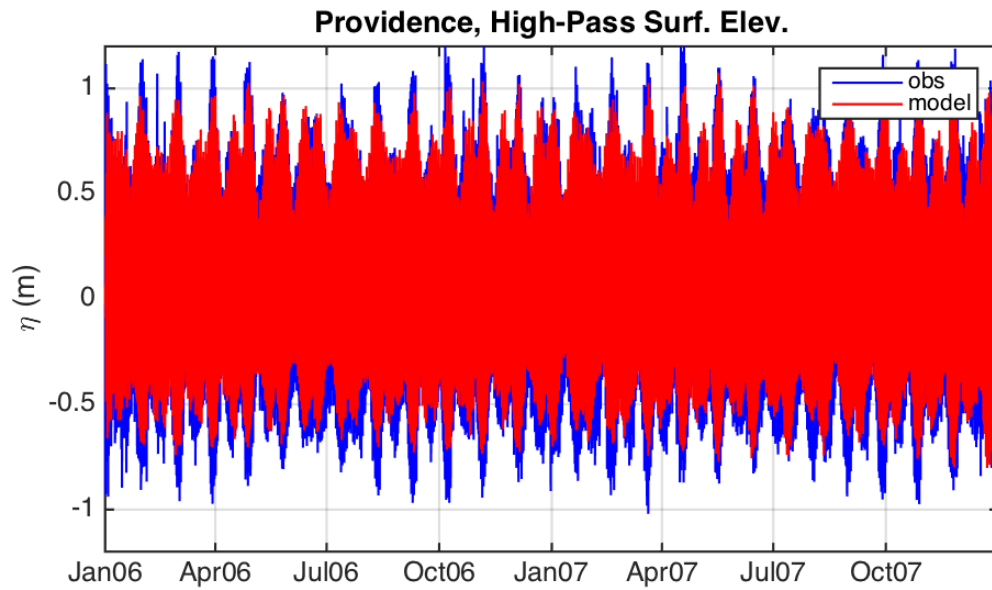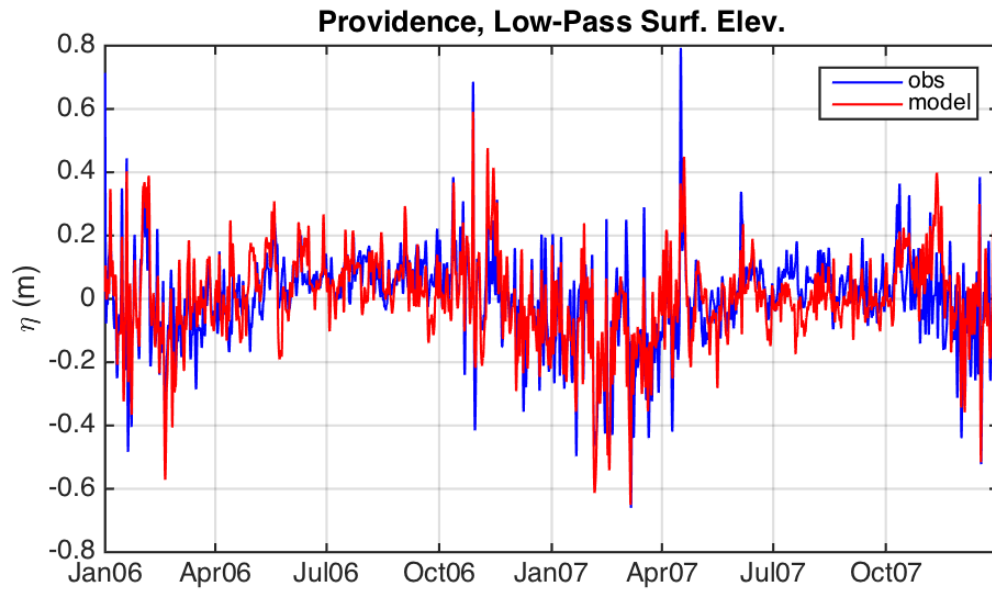
Figure 2.8: Comparison of surface elevation at Providence from model and observations. The time series are separated into (top) subtidal (low-pass filtered) and (bottom) tidal (hgh-pass filtered) frequency bands.

Low-Pass Filtered Surface Elevation

High-Pass Filtered Surface Elevation
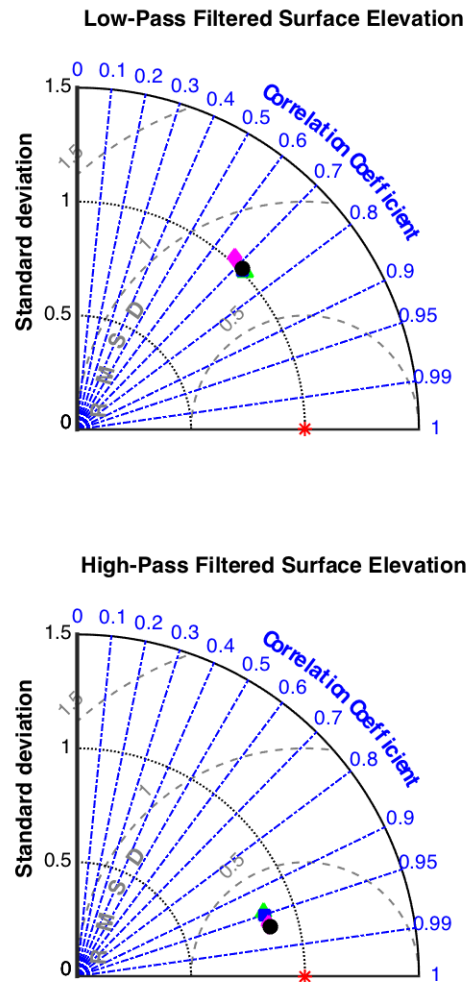
Figure 2.9: Taylor diagrams showing the performance of the model subtidal (top) and tidal (bottom) components of surface elevation. The red star represents the observations (a perfect model), and the model is denoted by the colored symbols: Providence = green triangles, Conimicut = blue squares, Quonset = magenta diamonds, and Newport = black circles.

2.2.2 Currents. Observations of currents were available at several locations in NB during 2006 and 2007. The measurements were made with bottom-mounted, upward-facing ADCPs at the sites shown in Figure 2.4. The duration of the observational records and the year in which they were obtained is given in Table 2.4. The ADCPs measured vertical profiles of the horizontal current every 10 or 60 minutes (see Table 2.4). The observed and modeled current profiles were vertically averaged and the time series were then filtered in the same way as the surface elevations to produce subtidal and tidal components. The direction of the major axis of variability was then determined for each component. The major axis directions for observed and model tidal currents differed by 4° or less, except at station EPs located in relatively shallow water (6.7 m depth) west of the main navigation channel, where the difference was 17° (Table 2.4). Major axis directions for the observed and modeled subtidal currents are within 2° for sites WP, EPc, and EP07, while the differences are 9° and 26° for sites EPs and MD07E respectively (Table 2.4). The observation-model comparisons described below were performed using the major axis current components (in the direction of the major axes) with model currents interpolated to the times of the observations.

As for surface elevation, observed and modeled currents are compared in both tidal and subtidal frequency bands. Visual comparisons of depth-averaged, major axis currents are shown in Figures 2.10-2.14. Although the details of the tidal phasing are not visible in these plots, it is evident that the model simulates the spring-neap variability in tidal amplitude well although the tidal amplitude is, in general slightly underpredicted by the model (as was seen for surface elevation). Subtidal current fluctuations, in general, are moderately well represented by the model, although the overall variability is slightly underpredicted at all sites.

Taylor diagrams visually illustrate the model performance in predicting depth-averaged currents in the tidal and subtidal bands (Figure 2.15). At tidal frequencies, certain sites (EPc and EPS) exhibit normalized standard deviations greater than 1 indicating overprediction of tidal variance, while for sites WP and EP07 the reverse is true. At MD07E, the model normalized standard deviation is almost exactly 1, indicating that the model and observations have the same tidal variance. Correlation coefficients between model and observed tidal currents range from 0.7 (WP) to nearly 0.9 (MD07E) and normalized rms differences are in the range of 0.5 − 0.8. Because the observation standard deviation in the tidal band is highly variable from site to site (Table 2.5), it is not possible to provide a single estimate of the absolute rms model-observation difference (product of the normalized rms difference from Figure 2.15 and the standard deviation from Table 2.5). The resulting rms differences are relatively large ($\sim$ 0.15 m/s) at sites with large tidal current variance (WP and EP07) and small ($\sim$ 0.05 m/s) at sites with small tidal current variance (EPc, EPs, and MD07E). Model skill for depth-averaged tidal currents range from 0.81 (WP) to 0.94 (MD07E).

At subtidal timescales, currents are generally underpredicted in magnitude, as indicated by the fact that the normalized sub-tidal standard deviations from the Taylor diagram are in the range of about 0.65 − 0.80 (Figure 2.15). Model-observation correlations in this frequency band range from about 0.35 at site EPs to 0.85 at EP07 suggesting that model performance depends strongly on location. The normalized

Station	Year	Duration (days)	$\Delta t_{samp.}$ (minutes)	θ_{hp}^{obs} (° true)	θ_{hp}^{mod} (° true)	θ_{lp}^{obs} (° true)	θ_{lp}^{mod} (° true)
WP	2006	112	10	41	39	45	43
EPc	2006	112	10	359	359	359	1
EPs	2006	56	10	8	351	358	349
EP07	2007	105	60	26	27	26	25
MD07E	2007	112	60	357	353	4	338

Table 2.4: Duration of instrument deployment, instrument sampling interval ($\Delta t_{samp.}$), and the direction of the major axis of variability of the high-pass (tidal) observed (θ_{hp}^{obs}) and modeled (θ_{hp}^{mod}) and the low-pass observed (θ_{lp}^{obs}) and modeled (θ_{lp}^{mod}) currents at the 5 ADCP sites.

rms model-observation differences are relatively small (~ 0.6) at the two sites in the East Passage channel (EPc and EP07) and large at the other sites ($0.8 - 1.0$). The subtidal standard deviations for the observations, from Table 2.5, are 0.05 m/s at the East Passage channel sites and 0.02 m/s elsewhere. Absolute rms differences are thus in the range 0.01 –0.03 m/s. Model skill at subtidal timescales are in the range 0.51 (EPs) to 0.85 (EPc).

Taken together, these comparisons indicate that tidal currents are moderately well simulated by the model, however the predictability is not nearly as good as for surface elevation. Subtidal currents are less well simulated than tidal currents, as was the case for surface elevation. The model skill values for both the tidal and subtidal bands still indicate, however, that the model exhibits useful predictive ability even if it is not as high as for surface elevation. The reduced predictability of model currents is likely due, at least to some extent, by inaccuracies in the model bathymetry. Currents can be strongly influenced by bathymetry, with strong bathymetric variability often giving rise to large spatial variability in currents. However, surface elevation is influenced less by bathymetric variability resulting in better predictability of this quantity.
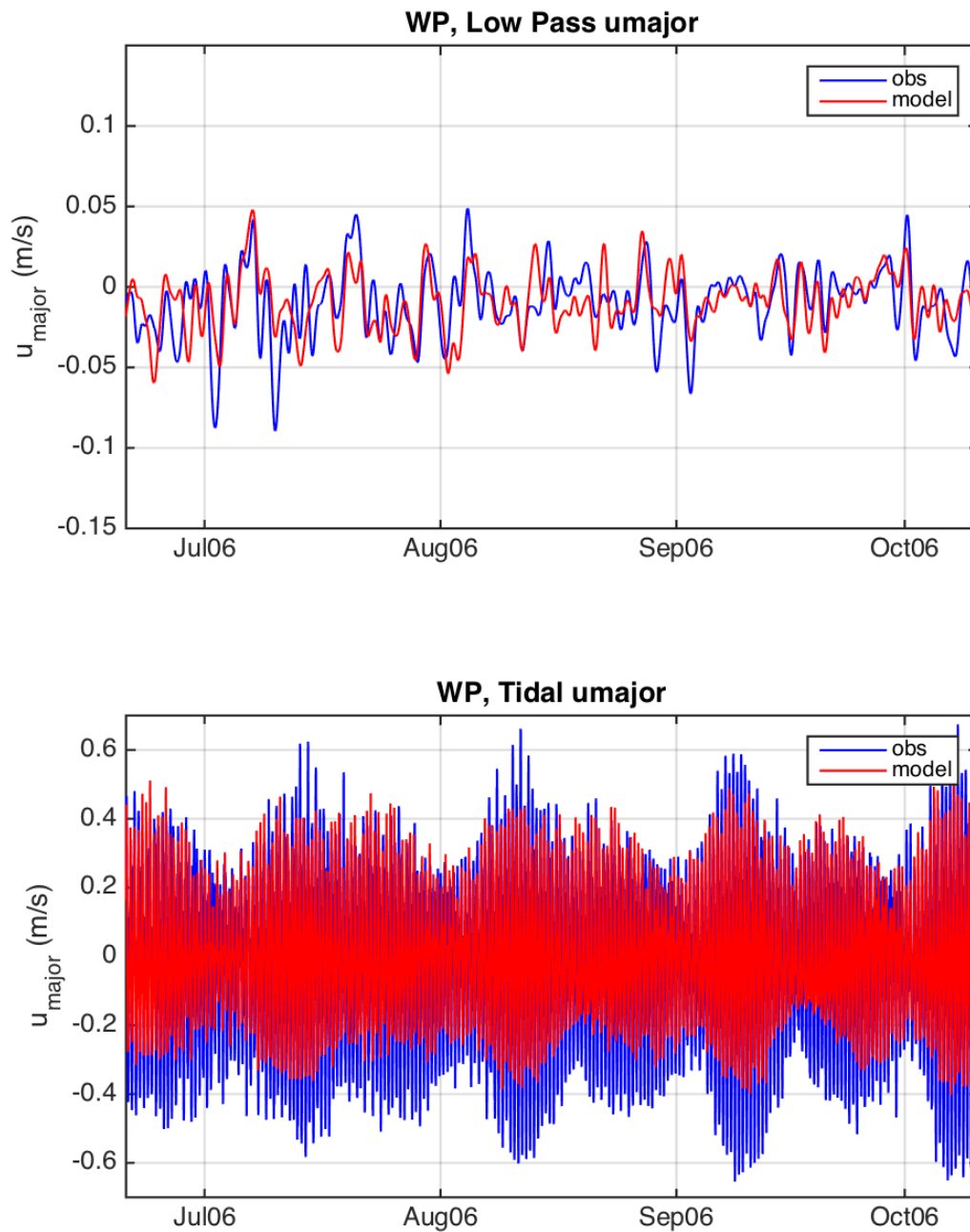
Figure 2.10: Comparison of depth-averaged major axis current at station WP from model and observations. The time series are separated into (top) subtidal (low-pass filtered) and (bottom) tidal (hgh-pass filtered) frequency bands.
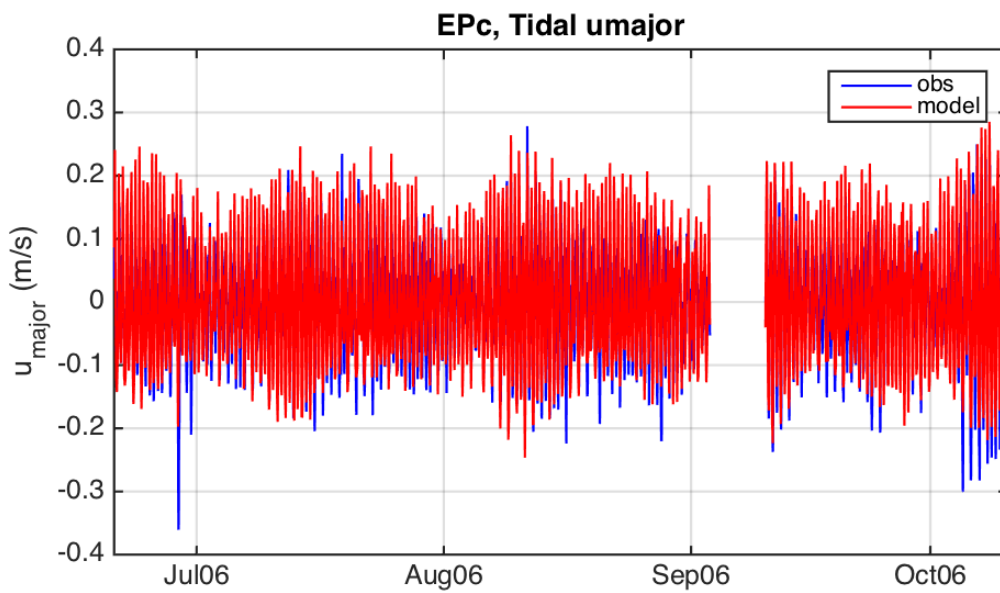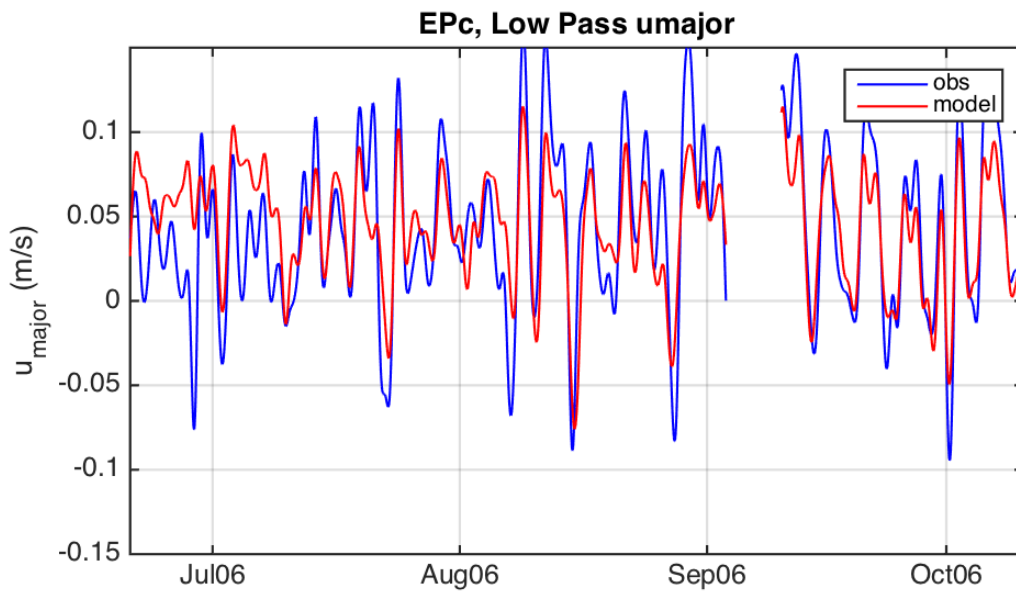
Figure 2.11: Comparison of depth-averaged major axis current at station EPc from model and observations. The time series are separated into (top) subtidal (low-pass filtered) and (bottom) tidal (hgh-pass filtered) frequency bands.
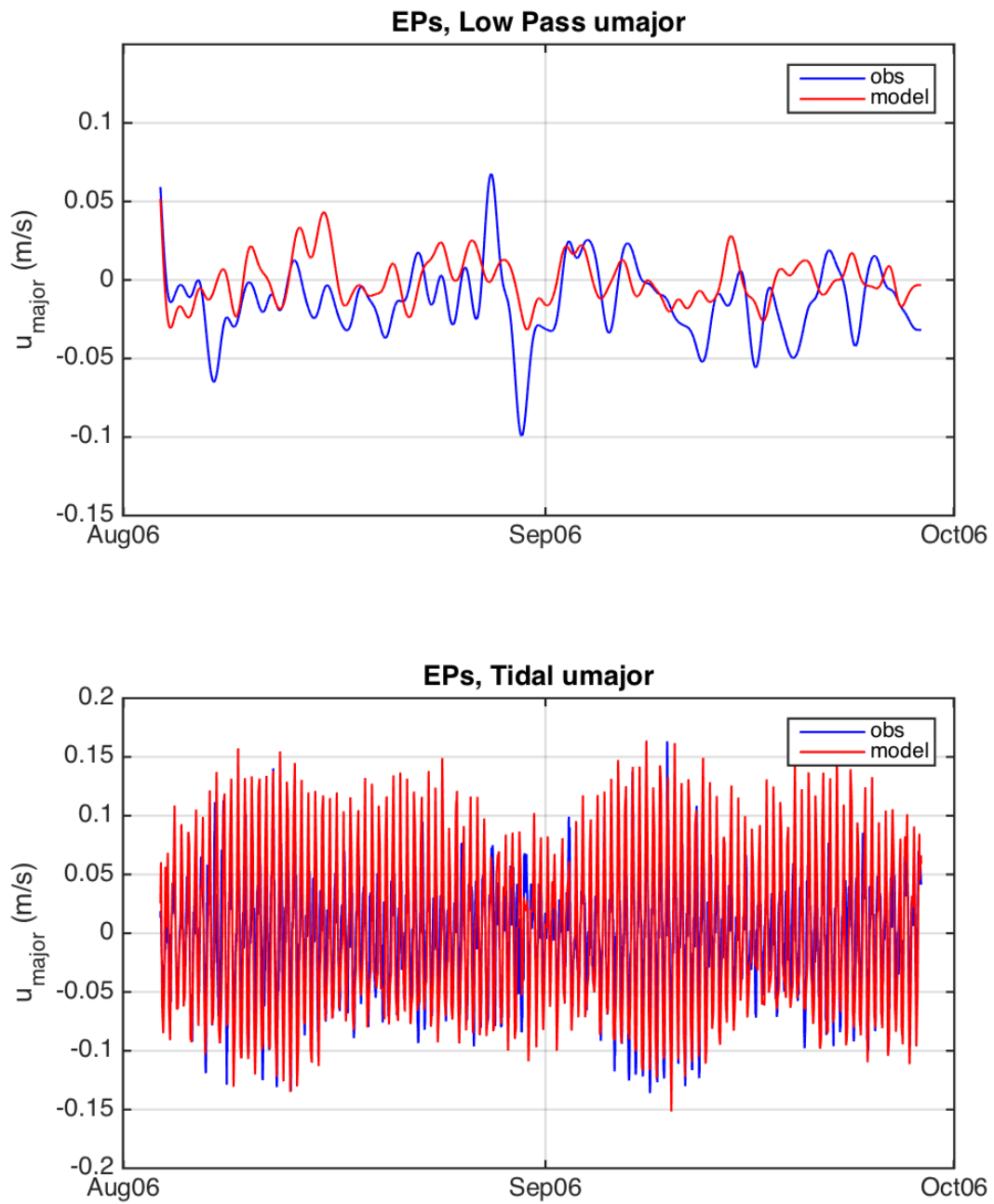
Figure 2.12: Comparison of depth-averaged major axis current at station EPs from model and observations. The time series are separated into (top) subtidal (low-pass filtered) and (bottom) tidal (hgh-pass filtered) frequency bands.
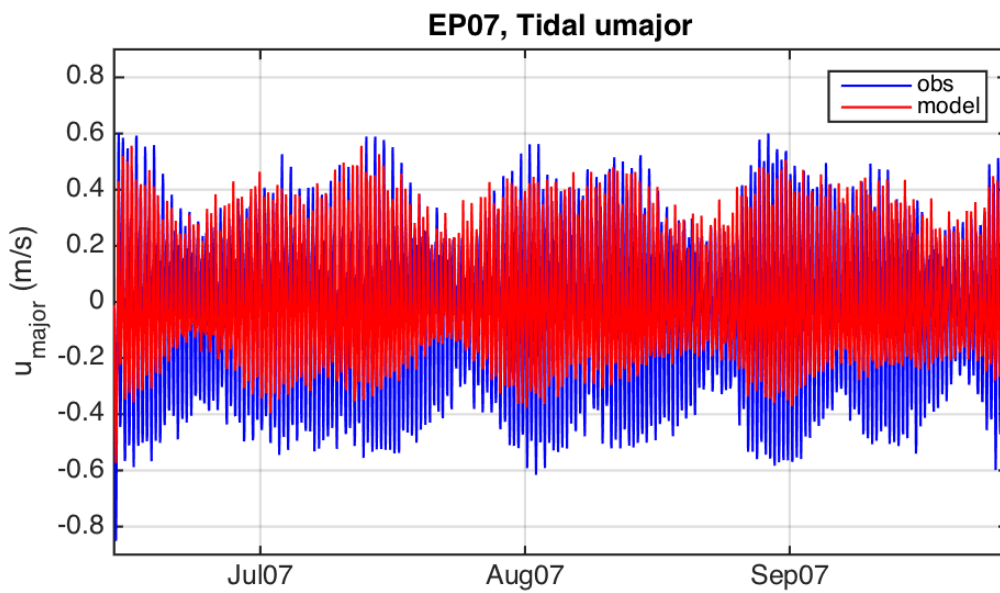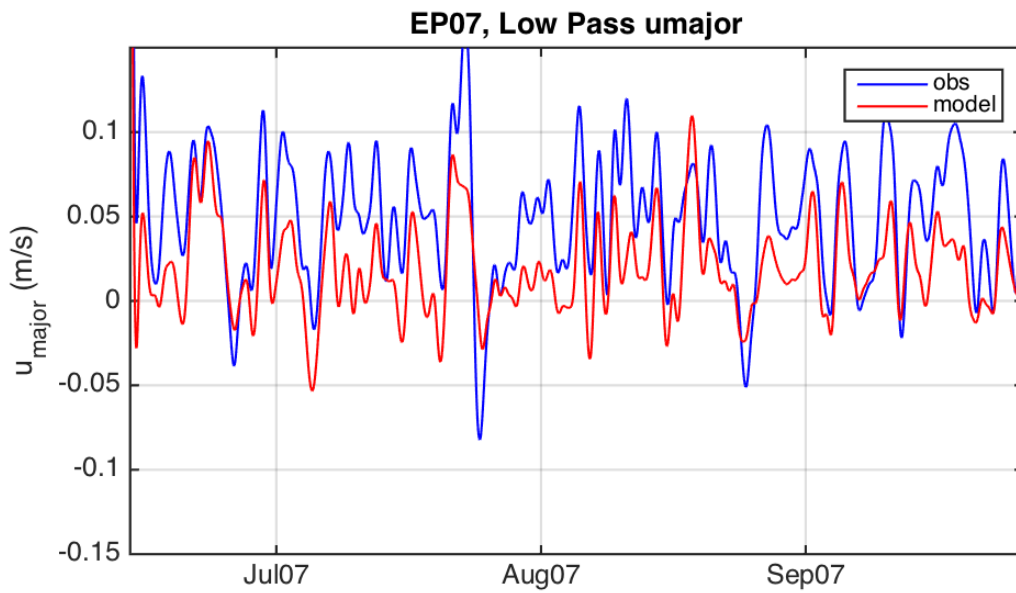
Figure 2.13: Comparison of depth-averaged major axis current at station EP07 from model and observations. The time series are separated into (top) subtidal (low-pass filtered) and (bottom) tidal (hgh-pass filtered) frequency bands.
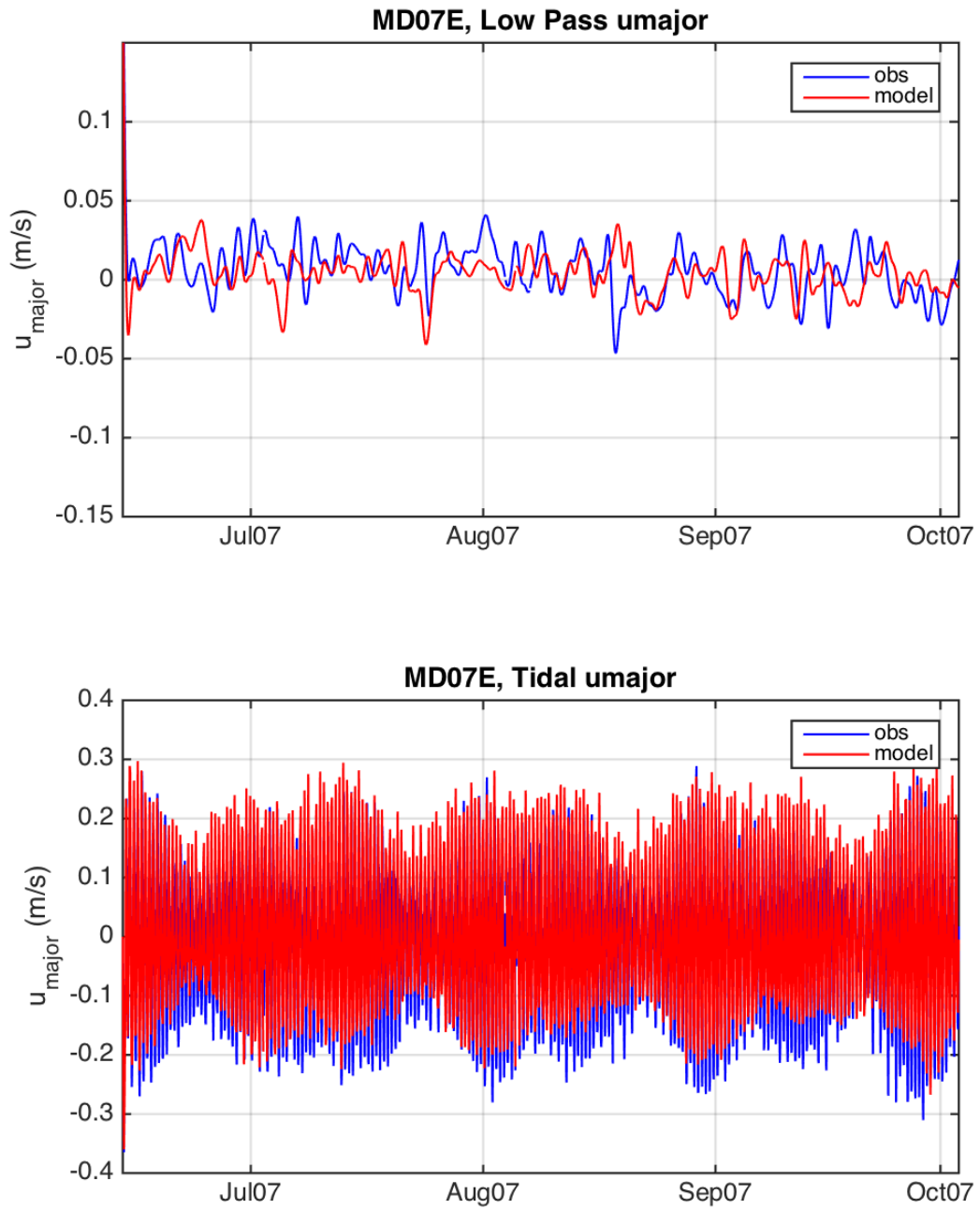
Figure 2.14: Comparison of depth-averaged major axis current at station MD07E from model and observations. The time series are separated into (top) subtidal (low-pass filtered) and (bottom) tidal (hgh-pass filtered) frequency bands.

Low-Pass Filtered Depth-Averaged Current

High-Pass Filtered Depth-Averaged Current
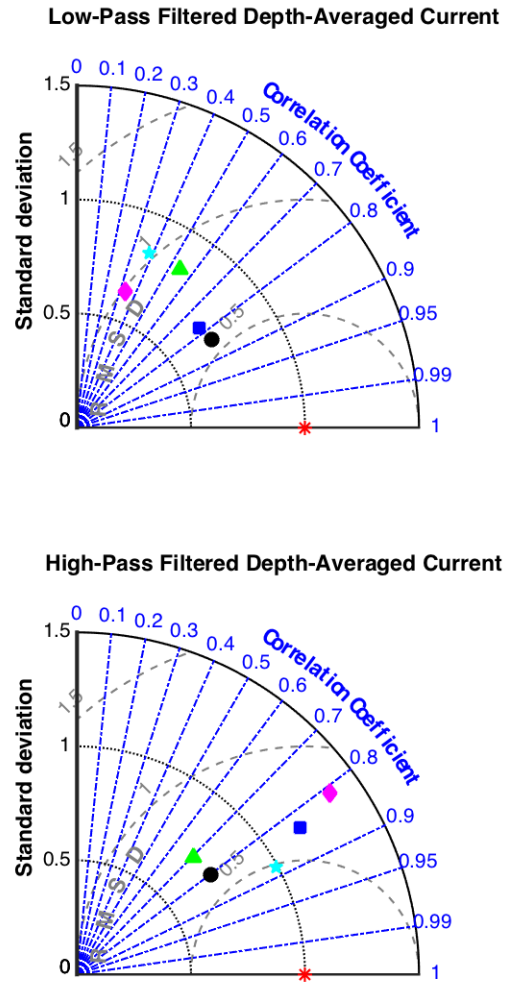
Figure 2.15: Taylor diagrams showing the performance of the model subtidal (top) and tidal (bottom) components of depth-averaged current in the major axis direction. The red star represents the observations (a perfect model), and the model is denoted by the colored symbols: WP = green triangles, EPc = blue squares, EPs = magenta diamonds, EP07 = black circles, and MD07E = cyan pentagrams.

Station	σ_tidal (m/s)	σ_subtidal (m/s)	Skill$_\text{tidal}$	Skill$_\text{subtidal}$
WP	0.26	0.02	0.81	0.72
EPc	0.08	0.05	0.91	0.85
EPs	0.05	0.02	0.88	0.51
EP07	0.29	0.05	0.87	0.78
MD07E	0.12	0.02	0.94	0.64

Table 2.5: Depth-averaged current standard deviations (σ) and model skill at tidal and subtidal timescales for each ADCP site.

2.2.3 Hydrography. Time series observations of temperature and salinity were obtained from the Narragansett Bay Fixed-Site Monitoring Network (NBFSMN; Codiga et al., 2009), an array of moored and dock-mounted sensors distributed throughout the mid and upper NB (Figure 2.4). At each site, measurements were made at 1 m below the surface and either 0.5 or 1 m above the bottom using Yellow Springs Instrument (YSI) sondes. At open water sites, the moorings were deployed only during the spring-fall period, while at 2 sites, Greenwich Bay Marina and T-Wharf (sites GB and TW in Figure 2.4), the observations were available throughout the year. The sondes sampled temperature and conductivity (in addition to other parameters) at 15 min intervals and these measurements allowed the computation of salinity. The raw data were averaged over 1-hour periods and the resulting hourly time series were used for the model validation. Because the temperature and salinity time series did not exhibit well defined tidal variability, the model-data comparisons are presented for the full records, with no separation into tidal and subtidal frequency bands as was done for surface elevation and currents.

Model simulated temperatures generally agree quite well with the values measured at the fixed sites (Figures 2.16-2.24). At most sites, not only is the seasonal cycle well simulated but the model, especially near the surface, also captures the fluctuations occurring on time scales of days to weeks. Bottom temperatures are slightly less well-simulated, and this is most apparent at the Bullock Reach site (Figure 2.16), where the model is several degrees too warm during the early summer of 2006. During this period, model surface temperature is slightly low, suggesting the possibility that model vertical mixing is too high at this location. At the sites in relatively deep water in mid-Bay (Popasquash Point, North Prudence, Mount View, Quonset Point, T-Wharf, and Mount Hope Bay) the model bottom temperature is slightly cold compared to the observations. This could be a result of the model vertical mixing being slightly too low (opposite to the situation at Bullock Reach) and not sufficiently mixing heat from the surface downwards or it could indicate an inaccurate specification of the deep temperature at the model open boundary (deep RIS waters are cool in comparison with waters in the Bay).

Taylor diagrams for temperature (Figures 2.25-2.26, left side) reinforce the general conclusion that the model simulates temperature very successfully. Normalized model standard deviations are close to unity, indicating that the model has the correct level of variability. Correlation coefficients between model and observed temperatures are above 0.9 with most above 0.95. Normalized rms differences are all below approximately 0.35, indicating that the model errors are small in comparison with the observed variability. Standard deviations of observed surface and bottom temperatures (Table 2.6) at sites without year-long measurements (all but T-wharf and Greenwich Bay) are in the range of 2.7–4.8 °C, indicating that at these sites, model temperature errors are generally in the range of 1–2 °C (note that although temperature standard deviations at T-Wharf and Greenwich Bay are higher because they experience the full annual cycle of temperature, the corresponding normalized rms errors are smaller than the values at the other sites, so that similar temperature errors are estimated). Model skill values for surface and bottom temperatures (Table 2.6) are all 0.94 or above, again indicating the generally high fidelity of the model temperatures.

The comparisons of model and observed salinities indicate that the model does not do as well in simulating salinity as it does for temperature. However, one should note that the determination of salinity requires measurement of conductivity, a measurement that is more difficult than temperature and can exhibit drift due to bio-fouling. In our experience the signature of bio-fouling of conductivity sensors is manifest by a decrease in the computed salinity. This occurs, for example, in the surface measurements at Quonset Point in late summer 2006 (Figure 2.22) and at Conimicut Point and Popasquash Point (Figures 2.17, 2.18) in late summer/early autumn of 2006. The fact that the surface salinity at other sites is unaffected during this period suggests the possibility of fouling-related errors in salinity at these sites. Another apparent anomaly is seen at the North Prudence site, where surface salinity in autumn 2006 abruptly jumps from below 30 to around 31 psu. Notwithstanding the possibility of errors in the observed salinity, we proceed below with the evaluation of model salinity.

In general, the model captures the annual cycle in salinity quite well. Lowest surface salinity occurs in early spring (2007) to late spring (2006), with highest salinity observed during summer. Near-bottom salinities exhibit a similar annual cycle, albeit with smaller amplitude of variability. At most sites, with the exception of Bullock Reach, the model correctly captures the magnitude of the annual cycle.

At Bullock Reach, model bottom salinity is much too low (by as much as 5 psu) during the late spring minimum of 2006 (Figure 2.16). Model surface salinity during that period is slightly high, supporting the suggestion above that the model vertical mixing is too strong there. At Greenwich Bay Marina, located close to the mouth of a small river entering Greenwich Bay, the model surface salinity does not exhibit the episodic low salinity episodes that the observations show (Figure 2.20) likely due to inadequacies in the specification of river discharge (see section 4.1). The model bottom salinity at that location exhibits a drop in autumn 2006 that is not seen in the observations. The surface salinity there (model and observations) decreases during this period. This suggests the likelihood that the model vertical mixing is too strong at this shallow location.

Figure 2.16: Time series of observed and modeled temperature and salinity at site BR. Shown top to bottom are surface temperature, bottom temperature, surface salinity, and bottom salinity.
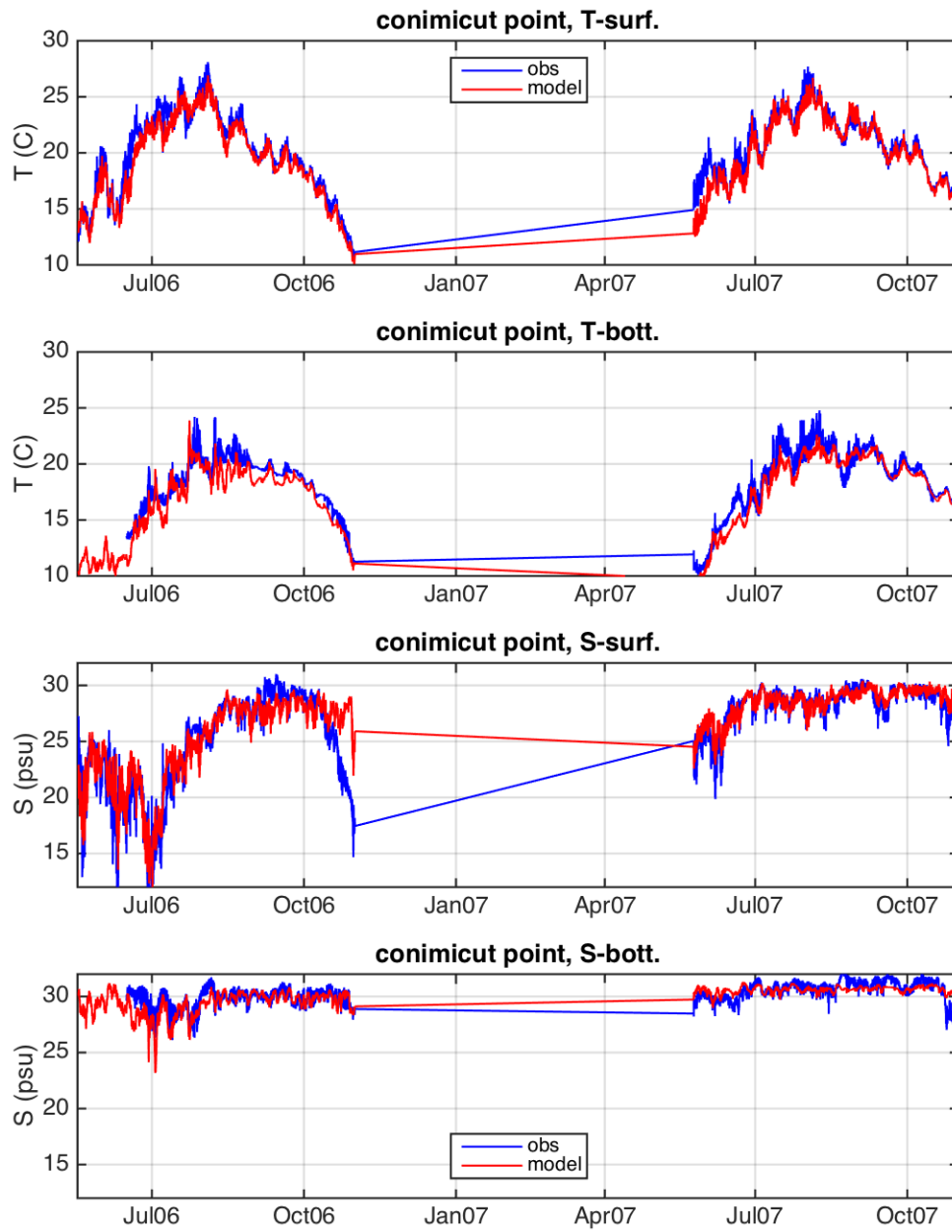
Figure 2.17: Time series of observed and modeled temperature and salinity at site CP. Shown top to bottom are surface temperature, bottom temperature, surface salinity, and bottom salinity.
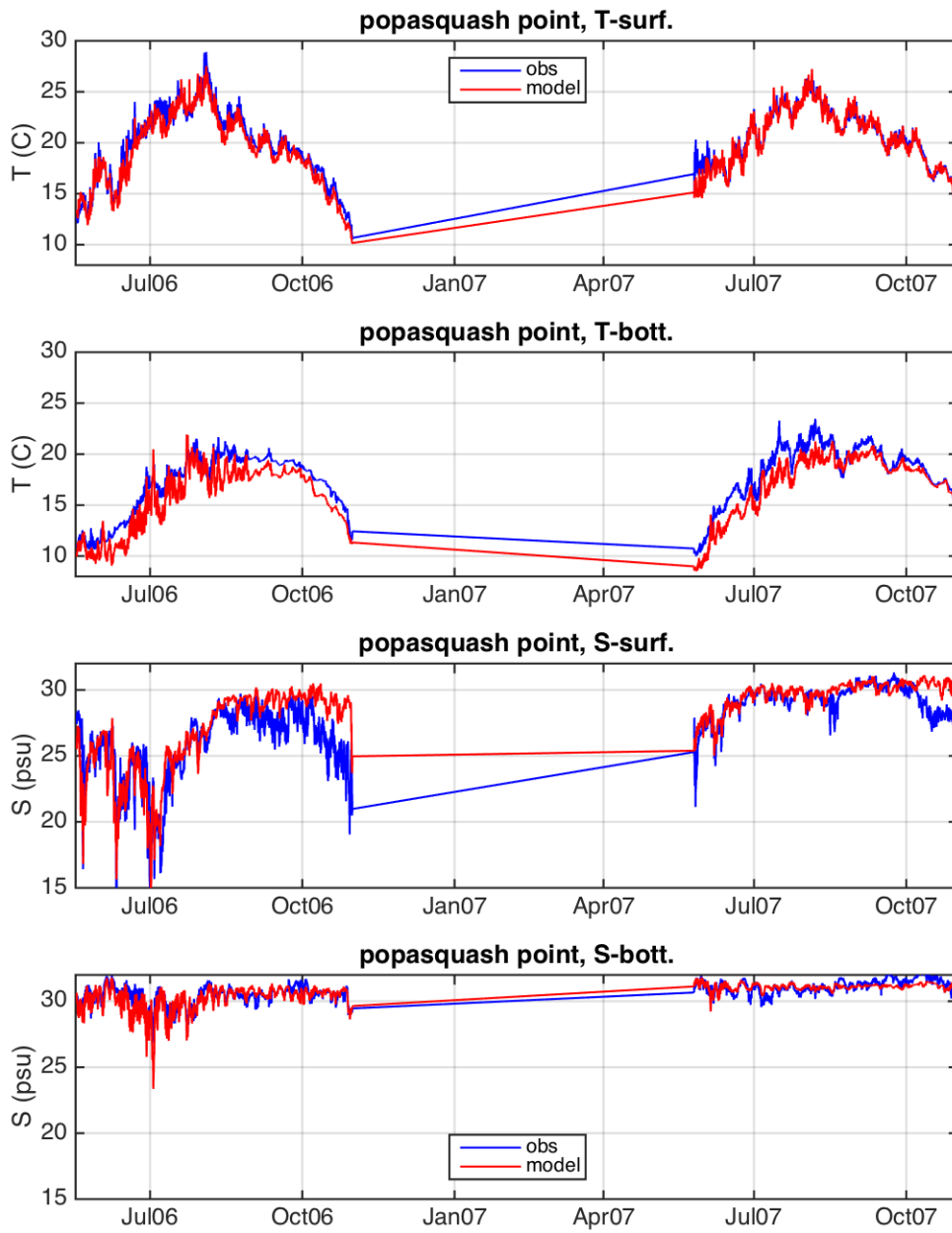
Figure 2.18: Time series of observed and modeled temperature and salinity at site PP. Shown top to bottom are surface temperature, bottom temperature, surface salinity, and bottom salinity.
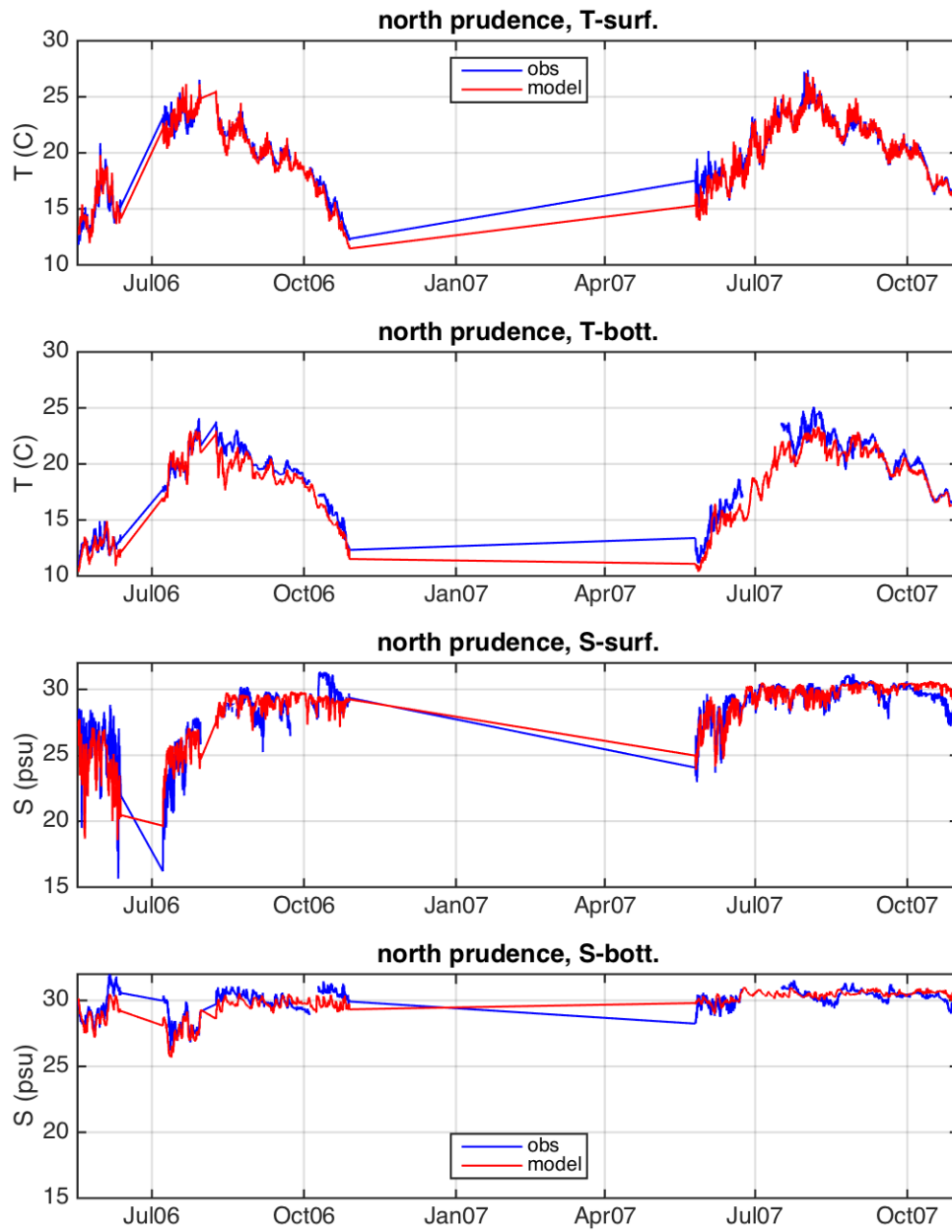
Figure 2.19: Time series of observed and modeled temperature and salinity at site NP. Shown top to bottom are surface temperature, bottom temperature, surface salinity, and bottom salinity.
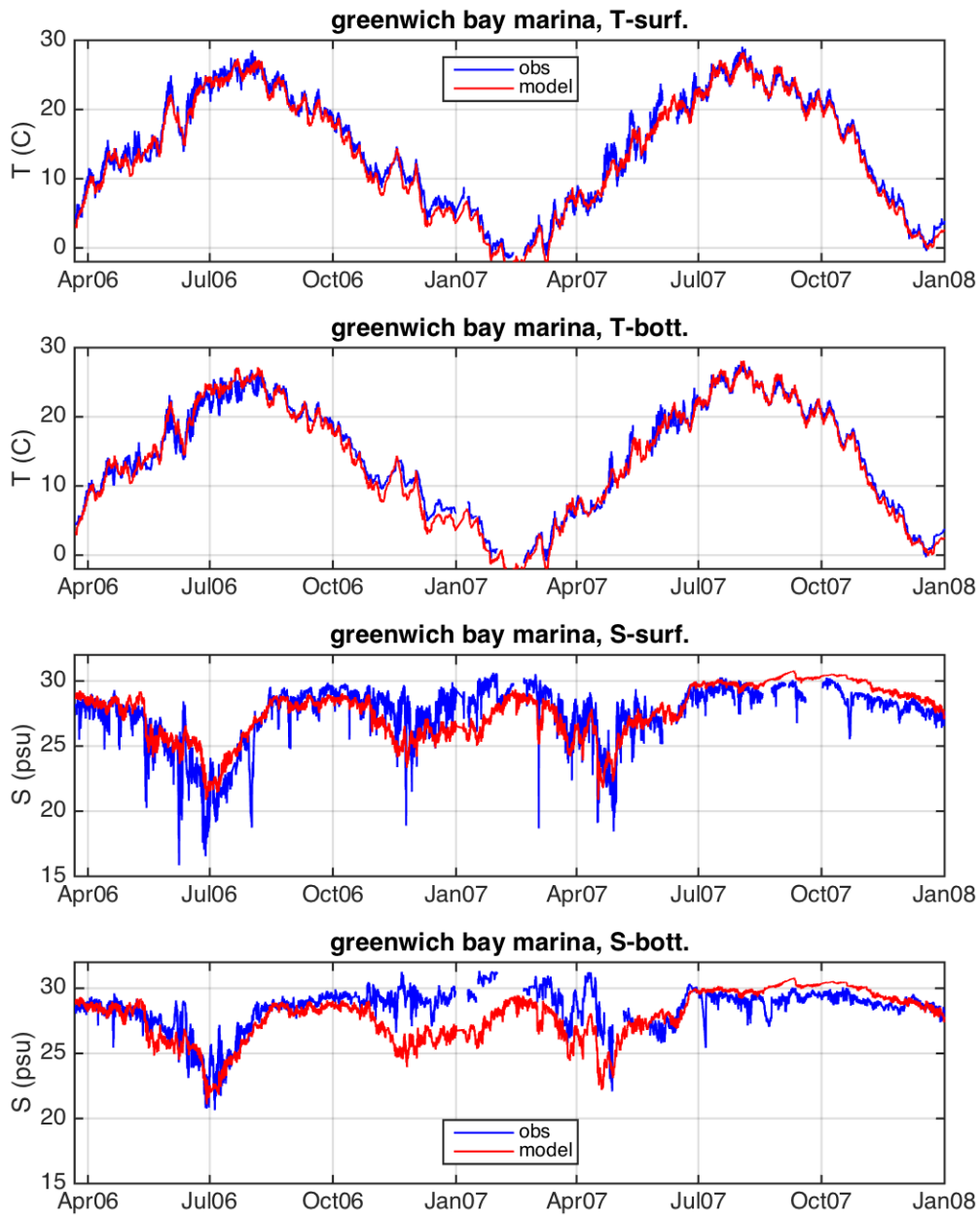
Figure 2.20: Time series of observed and modeled temperature and salinity at site GB. Shown top to bottom are surface temperature, bottom temperature, surface salinity, and bottom salinity.
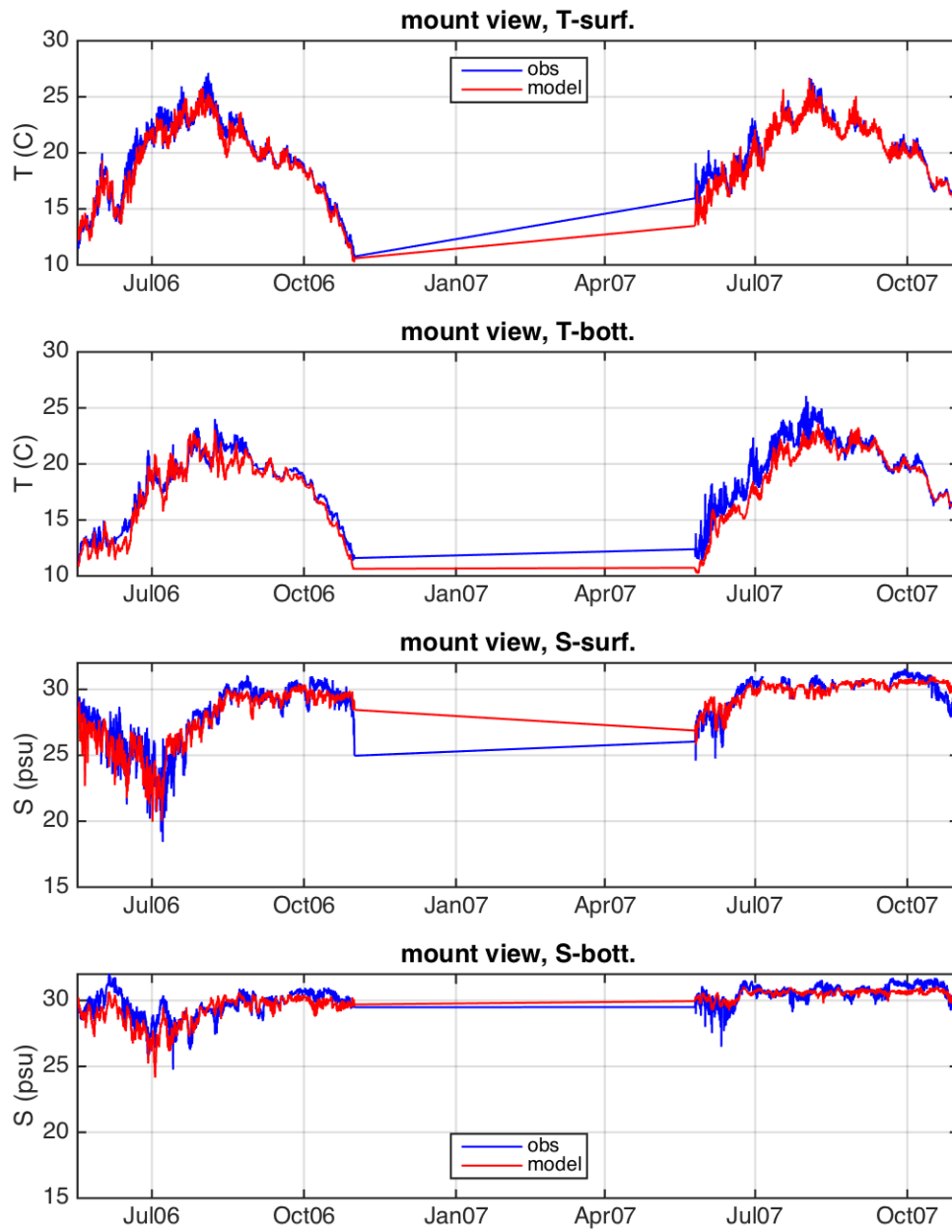
Figure 2.21: Time series of observed and modeled temperature and salinity at site MV. Shown top to bottom are surface temperature, bottom temperature, surface salinity, and bottom salinity.
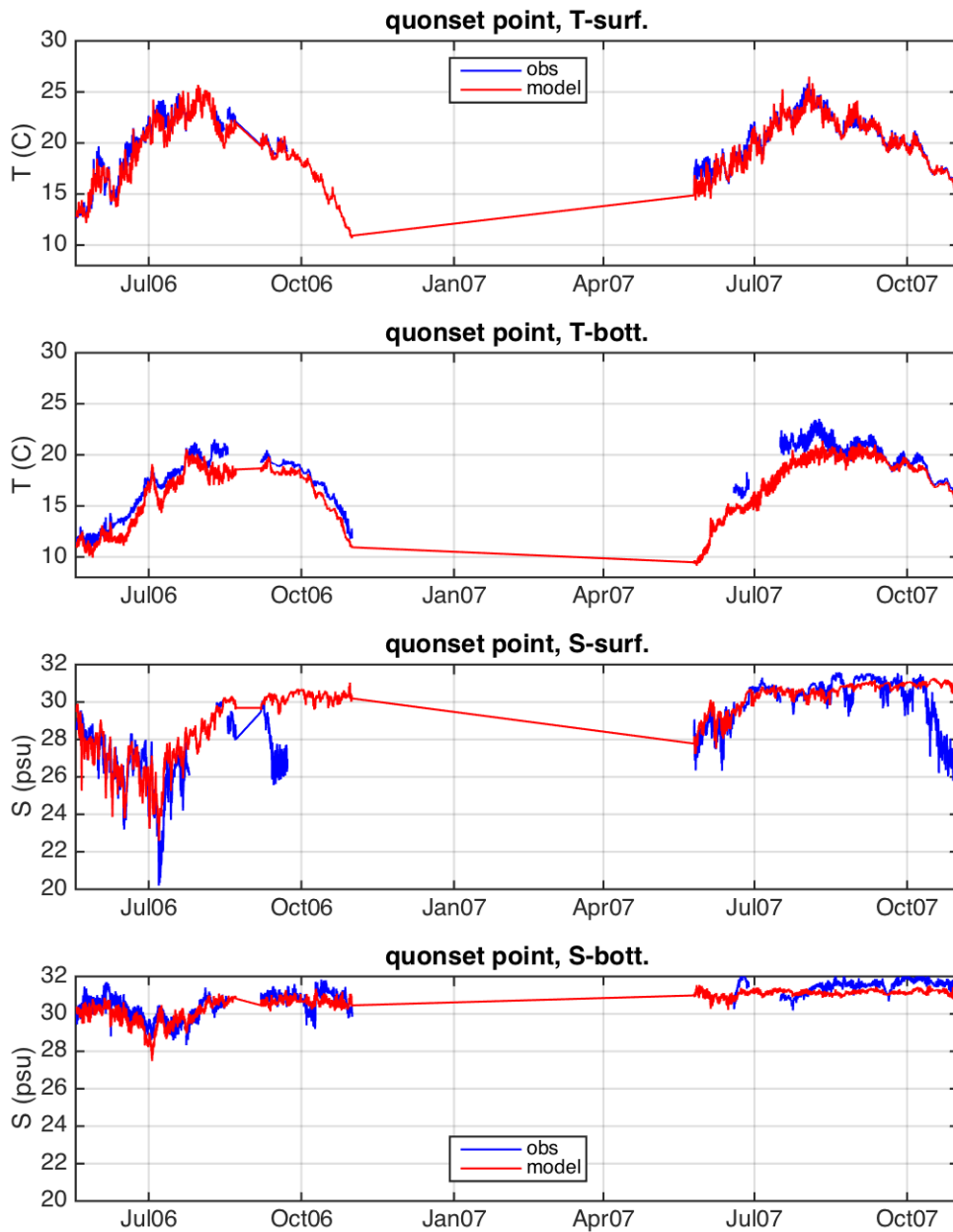
Figure 2.22: Time series of observed and modeled temperature and salinity at site QP. Shown top to bottom are surface temperature, bottom temperature, surface salinity, and bottom salinity.
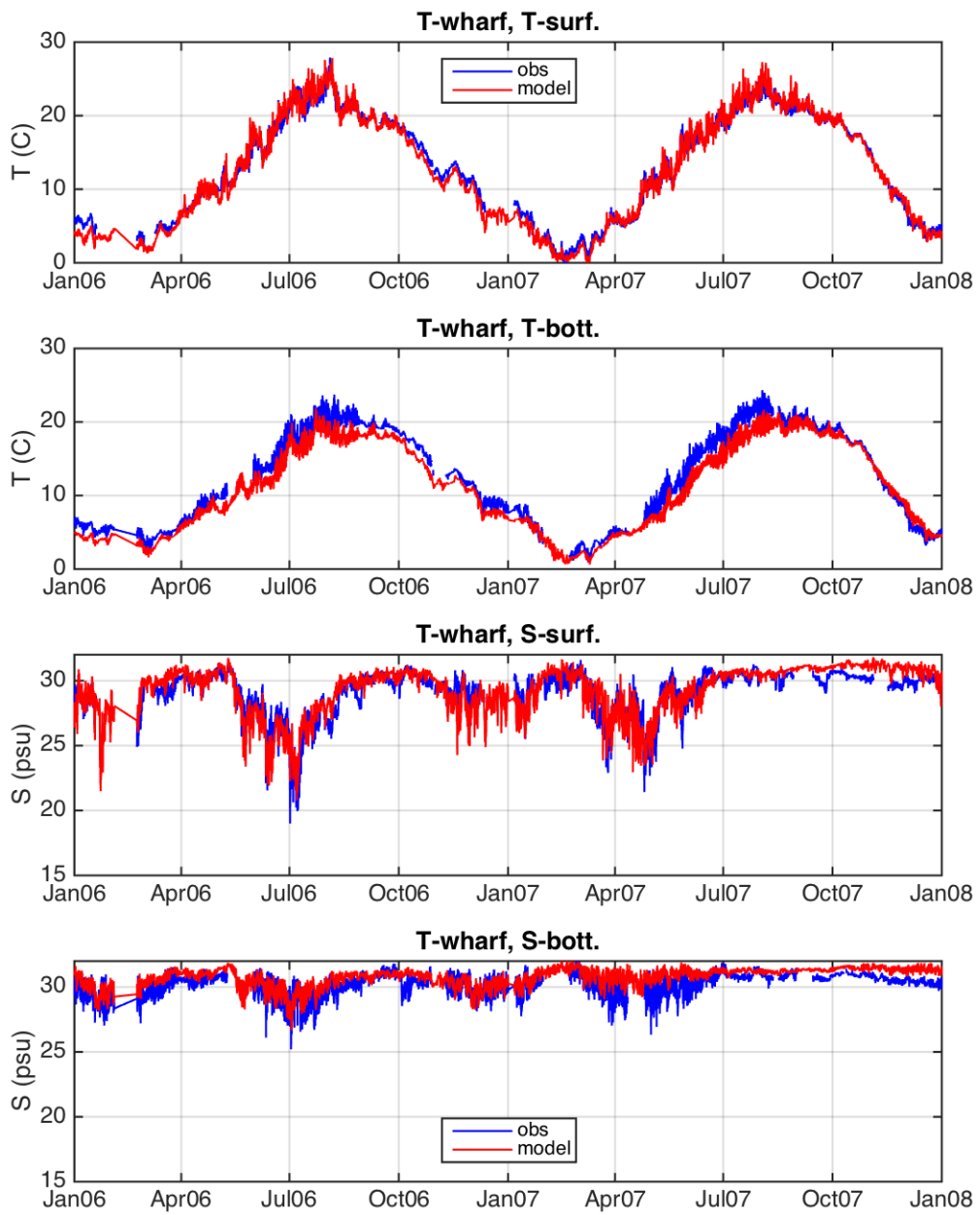
Figure 2.23: Time series of observed and modeled temperature and salinity at site TW. Shown top to bottom are surface temperature, bottom temperature, surface salinity, and bottom salinity.
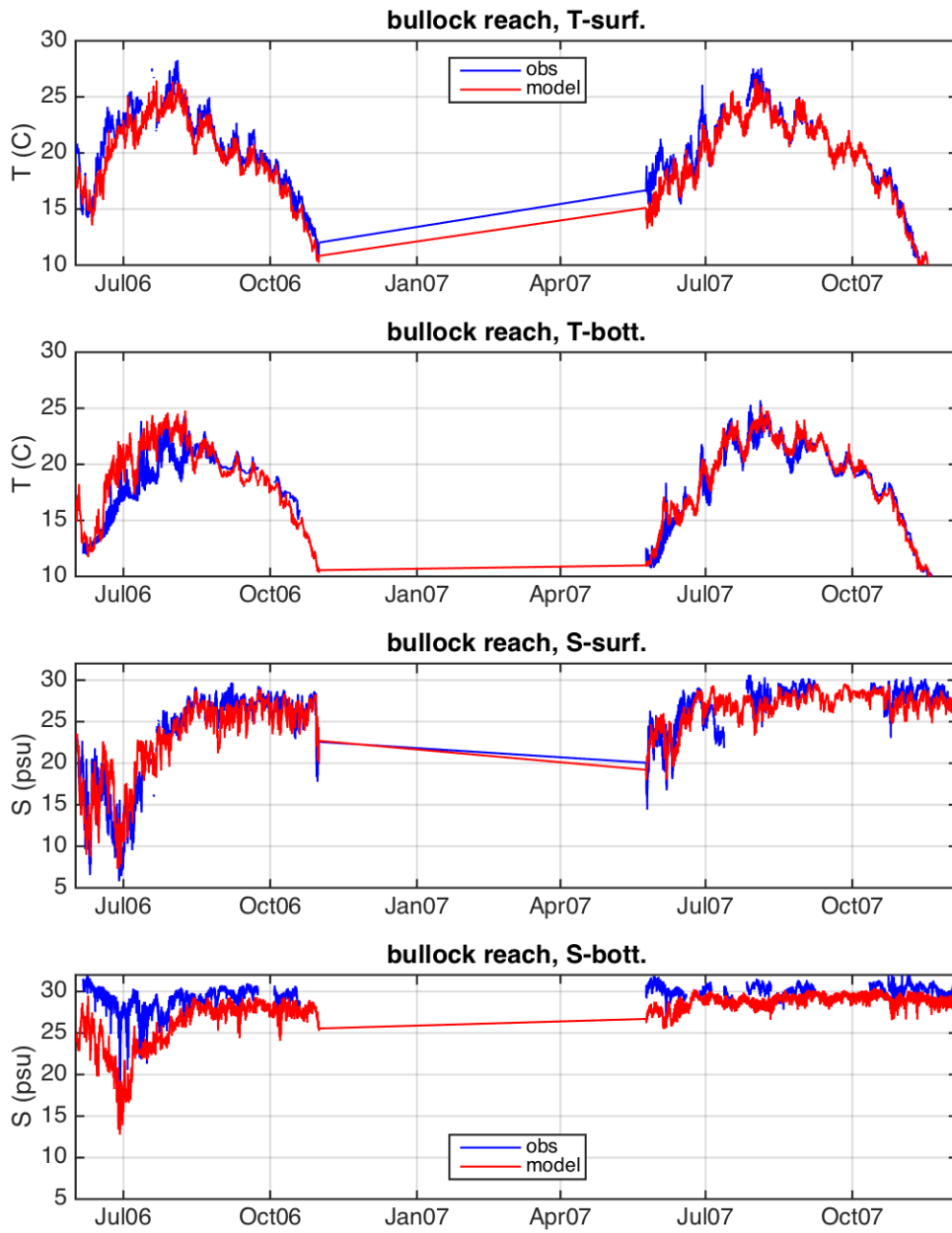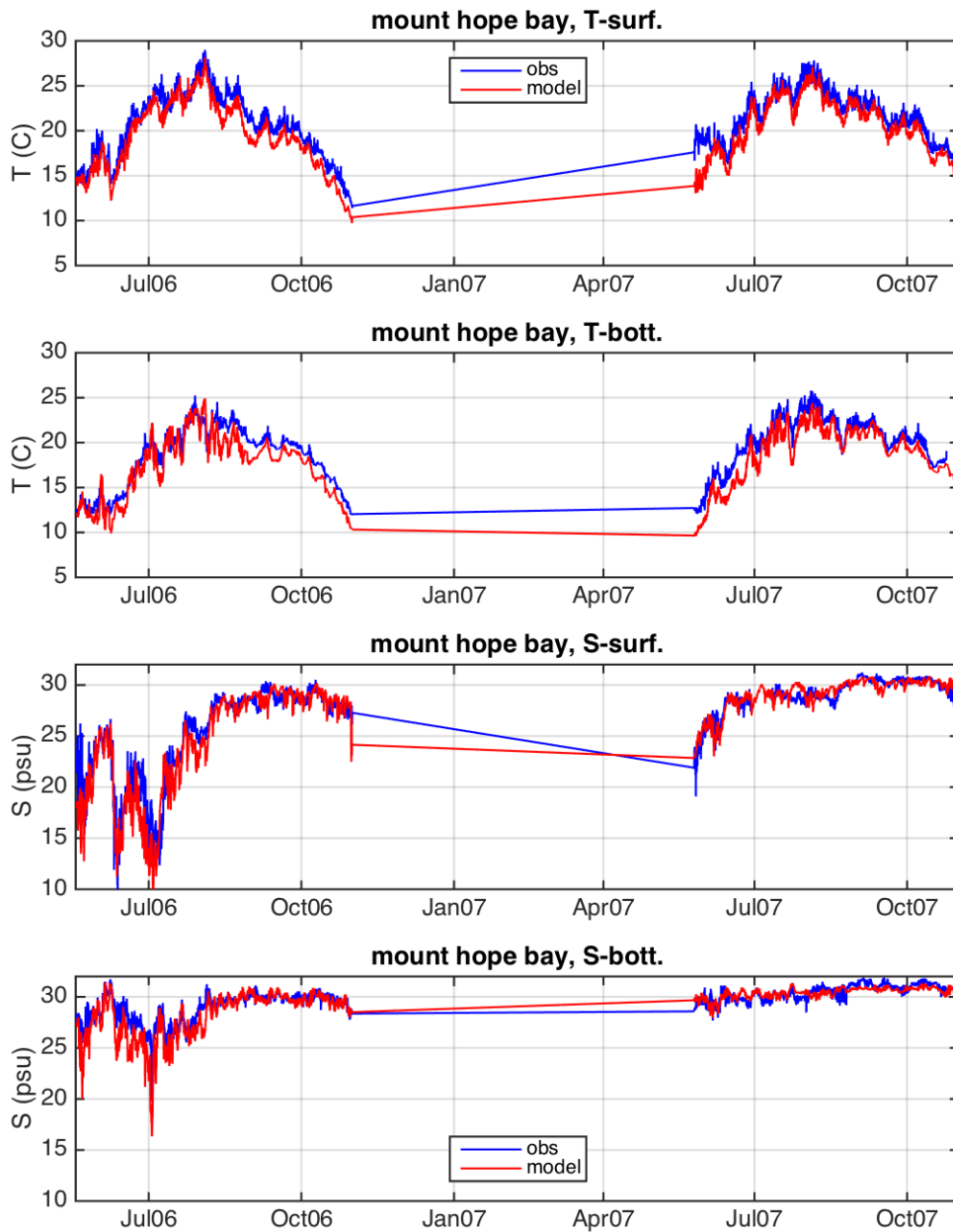
Figure 2.24: Time series of observed and modeled temperature and salinity at site MH. Shown top to bottom are surface temperature, bottom temperature, surface salinity, and bottom salinity.
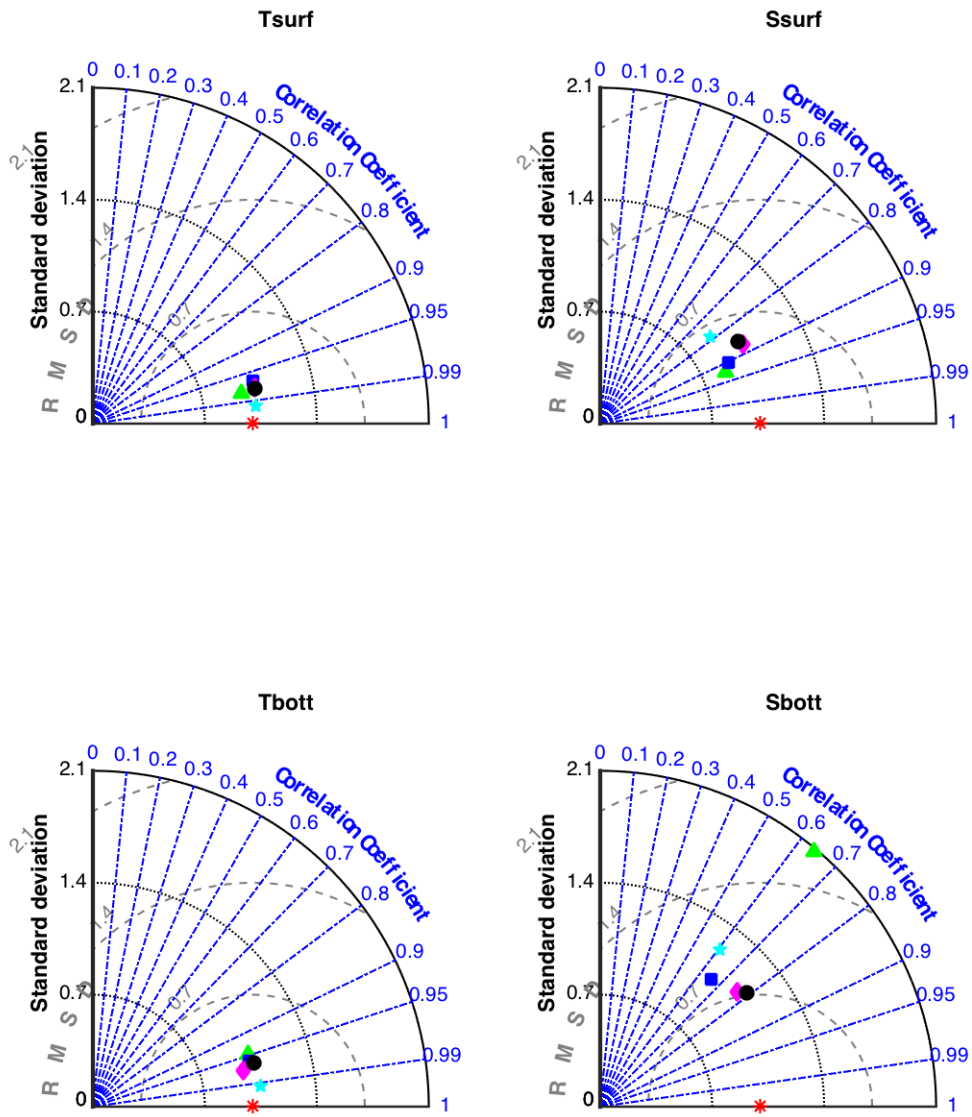
Figure 2.25: Taylor diagrams showing the performance of the model temperature (left) and salinity (right) at NBFSMN stations. The top and bottom rows show the results compared to the surface and bottom instruments respectively. The red star represents the observations (a perfect model), and the model results at the buoy locations are denoted by the colored symbols: BR = green triangles, CP= blue squares, NP = magenta diamonds, PP = black circles, and GB = cyan pentagrams.
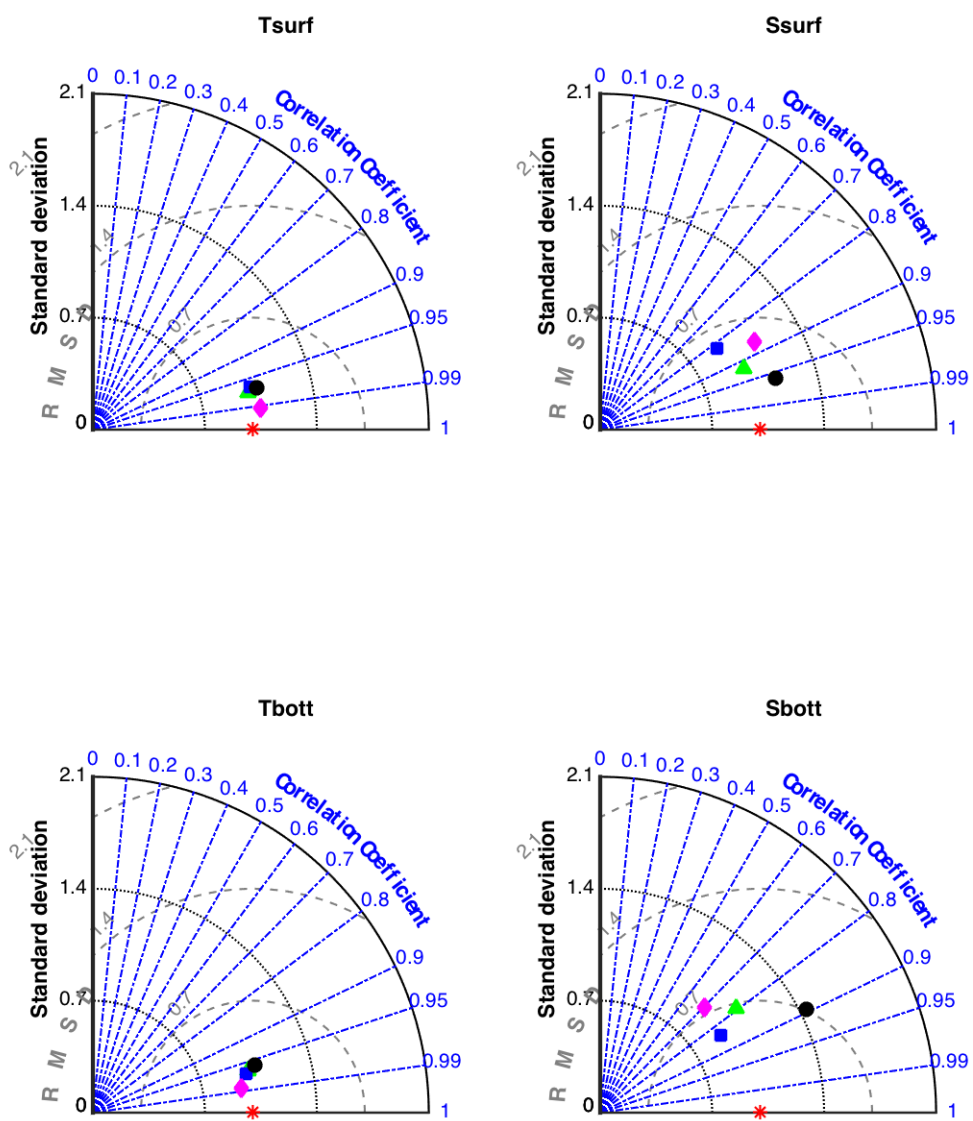
Figure 2.26: Taylor diagrams showing the performance of the model temperature (left) and salinity (right) at NBFSMN stations. The top and bottom rows show the results compared to the surface and bottom instruments respectively. The red star represents the observations (a perfect model), and the model results at the buoy locations are denoted by the colored symbols: MV = green triangles, QP= blue squares, TW = magenta diamonds, and MH = black circles.

Station	$\sigma_{\mathbf{T_s}}$ (^{o}C)	$\mathbf{Skill_{T_s}}$	$\sigma_{\mathbf{T_b}}$	$\mathbf{Skill_{T_b}}$ (^{o}C)	$\sigma_{\mathbf{S_s}}$	$\mathbf{Skill_{S_s}}$	$\sigma_{\mathbf{S_b}}$	$\mathbf{Skill_{S_b}}$
BR	4.8	0.98	4.2	0.97	5.0	0.95	1.4	0.52
CP	3.3	0.97	2.8	0.96	3.8	0.95	0.96	0.79
NP	3.2	0.99	3.4	0.98	2.1	0.93	0.86	0.87
PP	3.2	0.98	3.0	0.94	2.8	0.91	0.75	0.87
GB	8.1	0.99	7.7	0.99	2.3	0.88	1.5	0.75
MV	3.3	0.98	3.2	0.97	2.2	0.96	0.98	0.87
QP	2.7	0.98	2.9	0.96	2.1	0.89	0.74	0.87
TW	6.9	0.99	6.2	0.98	1.7	0.93	0.79	0.75
MH	3.3	0.95	3.2	0.95	4.0	0.97	1.4	0.90

Table 2.6: Temperature and salinity standard deviations (σ) and model skill for surface (T_s) and bottom (T_b) temperature and surface (S_s) and bottom (S_b) salinity for each NBFSMN site.

3 Parameterizing Physical Exchanges in Ecological Box Model (EcoGEM) using ROMS Dye Tracers

3.1 Box Model Methodology

The hydrodynamic model described in this report was used to parameterize the effects of physical exchanges in a 2-layer ecological model of NB. The ecological model, EcoGEM, was a coarse-resolution box model in which the NB was subdivided into 15 boxes (Figure 2.1). Each box consisted of an upper layer and a lower layer element with the interface between the layers set at a depth of 3.5 m below the mean water level. A so-called Gross Exchange Matrix (GEM), representing material transfers between each element and all other elements was determined using numerical simulations of dye tracers.

Exchanges between the 30 box model elements were quantified on a daily basis by initializing unique dyes with unit concentration in each element (and zero everywhere outside the element) and tracking the dyes over a full day. Evaluation of the dye inventory within individual elements at the end of the day allows for the computation of the fraction of dye originating in element i that ended up in element j. Likewise, each inflowing river in the model was tagged with a unique dye and the fraction of each river dye ending up in each element was computed. This procedure was repeated for every day of the two-year simulation (2006-2007), resulting in a time series of dye exchange fractions and river exchange fractions. The ecological box model equations describing the time variability of a dissolved or particulate constituent employ the resulting dye fractions to parameterize the inter-element exchanges and riverine inputs, assuming that the constituent behaves similarly to dye. For the ith model element the box model mass balance for a conservative tracer, including river inflows from K rivers, is:

$$C_i^{n+1}V_i^{n+1} = C_i^n V_i^n + \sum_{k=1}^{K} H_{k,i}^n C_k^{n,n+1} R_k^{n,n+1} + \sum_{j=1, j\neq i}^{J} F_{j,i}^n C_j^n V_j^n - \sum_{j=1, j\neq i}^{J} F_{i,j}^n C_i^n V_i^n, \quad (3.1)$$

where $H_{k,i}^n$ is the fraction of the kth river dye found in the ith element after 1 day, $C_k^{n,n+1}$ and $R_k^{n,n+1}$ are the concentration and volume flux of the kth river over the 1-day time step, $F_{i,j}$ is the fraction of the ith dye, originating in the ith element, that is found in the jth element after 1 day, C_i and V_i are the concentration in and volume of the ith element, and the superscripts refer to the time step. In equation 3.1, the second term on the right hand side (RHS) represents river inputs while the third and fourth terms on the RHS represent respectively the material transfers from all other elements to the ith element (gains) and the transfers from the ith element to all other elements (losses).

In addition to the physical processes parameterized in equation 3.1 using the dye fractions, the equations for the ecological variables in the EcoGEM box model also

include biological processes (not shown). To verify the parameterized physical processes, the box model equation (equation 3.1) was used, with the daily dye exchange fractions, to simulate a conservative tracer, the time-varying salt mass and salinity within box model elements. Figure 3.1 shows a comparison of the results for the surface (3S) and bottom (3B) elements of box 3. Shown in blue are the integrated values (over the elements) from the ROMS simulation, while the red lines denote the values simulated using the box model. The comparison is quite good, indicating the basic soundness of the approach. The discrepancies between the ROMS and EcoGEM time series are likely a result of discretization errors due to the long timestep (1 day) used for the box model simulation.

The use of a 24-hour time period for the individual dye simulations was, in retrospect, not an optimum choice (see the discussion below). Because many of the biological parameterizations were based on daily observations, the ecological model was formulated to use a daily timestep for the physical exchanges. As NB is a strongly tidally-forced system, we originally performed the dye-exchange model runs using a duration of 24.84 h (two M_2 tidal cycles), so that the exchanges would represent net non-tidal exchanges. As a test of the GEM method, we simulated the time-varying salt mass (a conservative tracer) within each element using equation 3.1 and compared the result with the actual salt mass within the model element (integrating the model salinity over the element). However, using the dye fractions from the 24.84-hour simulations in equation 3.1, we could not, using a 24-hour box model timestep, reproduce the (known from the model simulation) time-varying salt mass variability within box model elements. The solution to this problem was to perform the dye exchange simulations over exactly 24 hours. Using 24-hour dye fractions, the time-varying salt masses within elements could be accurately simulated as shown in Figure 3.1 and in Kremer et al. (2010), thus demonstrating the physical consistency of the dye exchange approach.

3.2 Variability in Dye-Exchange Fractions

The dye-exchange fractions derived from the 1-day model runs exhibit a high degree of temporal variability. This is due to fluctuations in circulation and mixing associated with meteorological and riverine variability as well as the methodological artifact resulting from the 24-hour duration of the dye-exchange model runs.

Example time series of dye-exchange fractions for EcoGEM elements from box 3 (surface and bottom elements, denoted as 3S and 3B), located in the lower portion of the Providence River (see Figure 2.1), are shown in Figure 3.2. Note that the dye-exchange fractions shown do not sum to unity because, typically, dye remains in the source element and also a small quantity of dye is found in other box model elements (these are not shown in Figure 3.2 for clarity). For dye release in element 3S (top panel in Figure 3.2), the largest fraction of dye is lost to elements 4S and 5S, the surface elements immediately seaward, with smaller fractions lost to element 3B and element 2S (the surface element immediately landward of 3S). For dye release in element 3B (bottom panel in Figure 3.2), the largest fraction of dye is lost to

element 3S, with a smaller fraction ending up in element 2B (the bottom element immediately landward) and a small fraction lost to elements 4B and 5B (bottom elements immediately seaward). The pattern of down-estuary exchange near the surface and up-estuary exchange near the bottom indicates the importance of the estuarine circulation (seaward flow near the surface and landward flow at depth) at this location in the estuary. Vertical exchange is significant at this location but, as is the case with all of the exchange fractions shown, there is significant temporal variability.

The dominant timescales associated with the variability in dye exchange shown in Figure 3.2 are examined by computing power spectra of the dye-exchange time series. The spectra, which were band-averaged over 15 frequencies, are shown in both log-log form (Figure 3.3) and variance-preserving form (Figure 3.4). The former shows that the spectra are, in an overall sense, nearly "white" (approximately equal spectral density over the entire resolved frequency range). Many of the individual spectral peaks are significant at the 95% level. The variance-preserving plot shows that the high frequency (shorter period) fluctuations, at periods less than about 20 days, dominate the overall signal variance. Fluctuations in dye-exchange at periods shorter than 10 days are mainly due to changes in circulation and mixing forced by meteorological variability.

Particularly noteworthy in Figures 3.3 and 3.4 are the spectral peaks centered at approximately 14-day periods for dye-exchange from element 3S to 2S and 4S/5S and from 3B to 2B and 3S. The 14-day period is significant because, for a semi-diurnal tidal regime like NB, this is the period over which tidal phase varies (for example, maximum flood occurs at the same time of day every 14 days). We hypothesize that dye-exchange for a 24-hour simulation is strongly dependent on the tidal phase at the time of release (midnight). If this is the case, then the dye exchange fractions would be expected to fluctuate in magnitude with a 14-day period as observed. It is possible that the observed 14-day periodicity in dye exchange fractions could be due to fortnightly spring-neap variability in tidally forced vertical mixing. However, in NB, the main spring-neap periodicity occurs at the monthly timescale (see, for example, Figure 2.5) and the spectra do not generally exhibit peaks at this period. This suggests that the 14-day variability in dye-exchange fractions arises as an artifact of the methodology whereby dye is released each day at midnight and is tracked for exactly 24 hours.

Based on the indication of spurious variability in exchange fractions at 14-day periods using 1-day dye exchange fractions, it is suggested that future implementations of the dye-exchange methodology for forcing ecological box models use a smaller window over which the exchange is computed. This time window should be short enough (e.g. 1-2 hours) to resolve tidal variability of both mixing and advection.
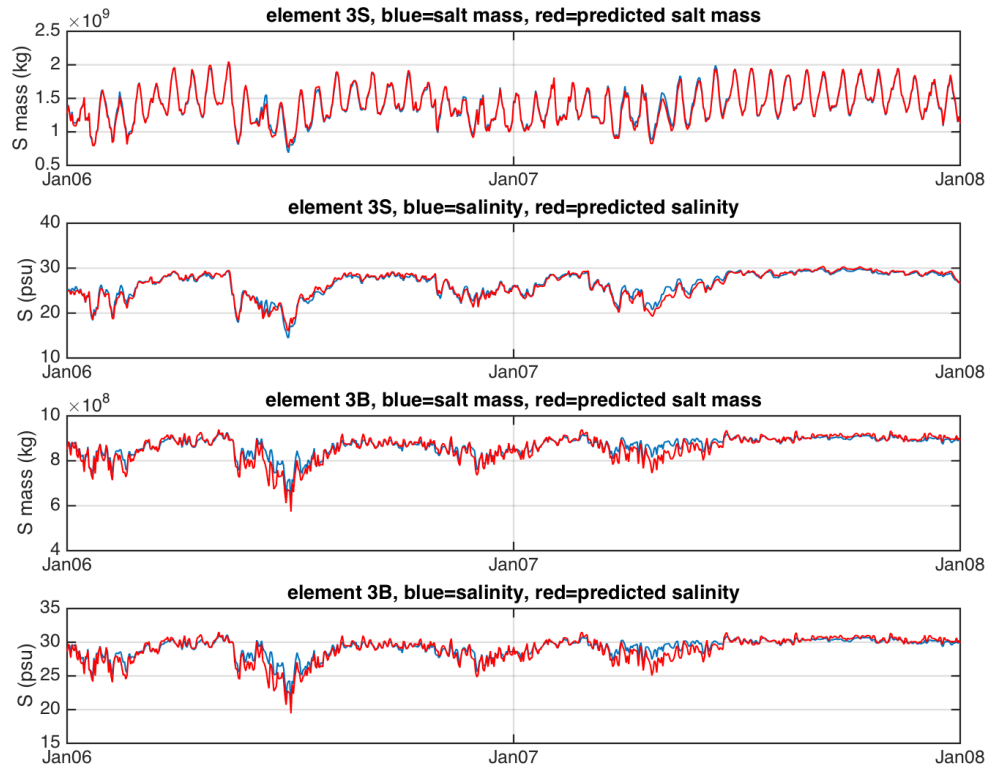
Figure 3.1: Time series of daily salt mass and salinity (at midnight) in the surface element of box 3 (top two panels) and the bottom element of box 3 (bottom two panels). The values from the ROMS simulation are shown in blue and the values predicted from the box model (equation 3.1) are shown in red. The pronounced spring-neap (~14 day) variability in the salt mass in the surface element is due to the variability in the element volume at midnight as the tidal phase varies over the spring-neap cycle. See Figure 2.1 for the location of EcoGEM box 3.

Figure 3.2: Time series of daily dye exchange fractions for numerical dyes released from the surface (top panel) and bottom (bottom panel) elements in EcoGEM box 3 (see Figure 2.1 for the box location.)

Figure 3.3: Power spectral density (PSD) of daily dye exchange fraction time series for numerical dyes released from the surface (top panel) and bottom (bottom panel) elements in EcoGEM box 3 (see Figure 2.1 for the box location). The vertical dotted lines indicate periods of 3, 7, and 14 days.
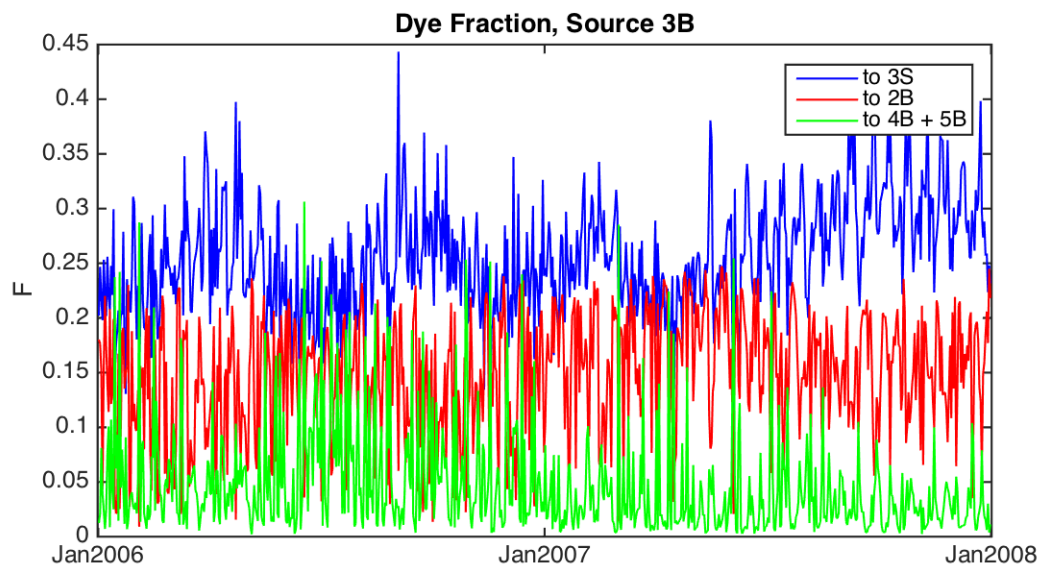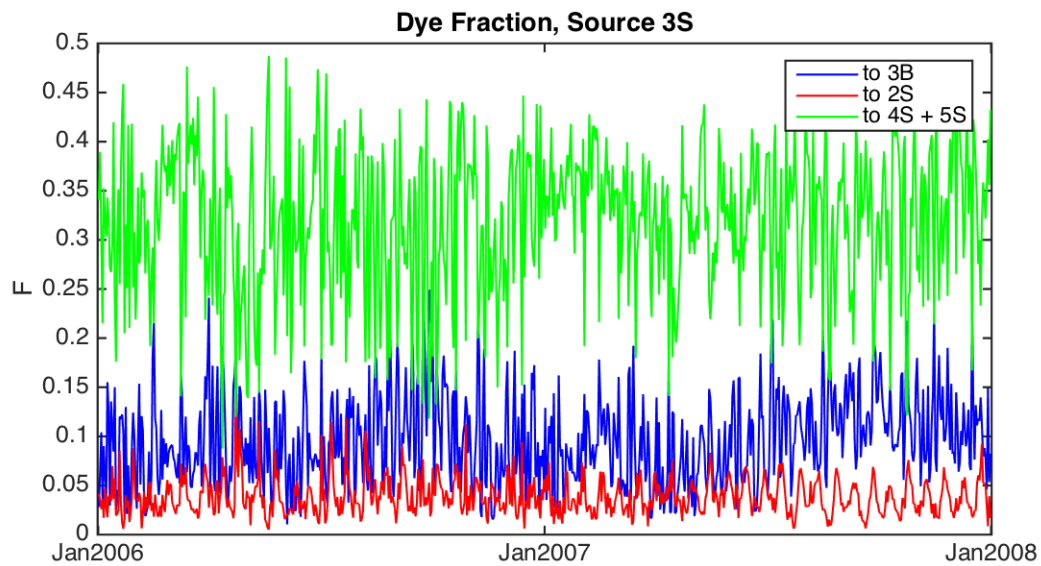
Figure 3.4: Variance-preserving plots of power spectral density (PSD) of daily dye exchange fraction time series for numerical dyes released from the surface (top panel) and bottom (bottom panel) el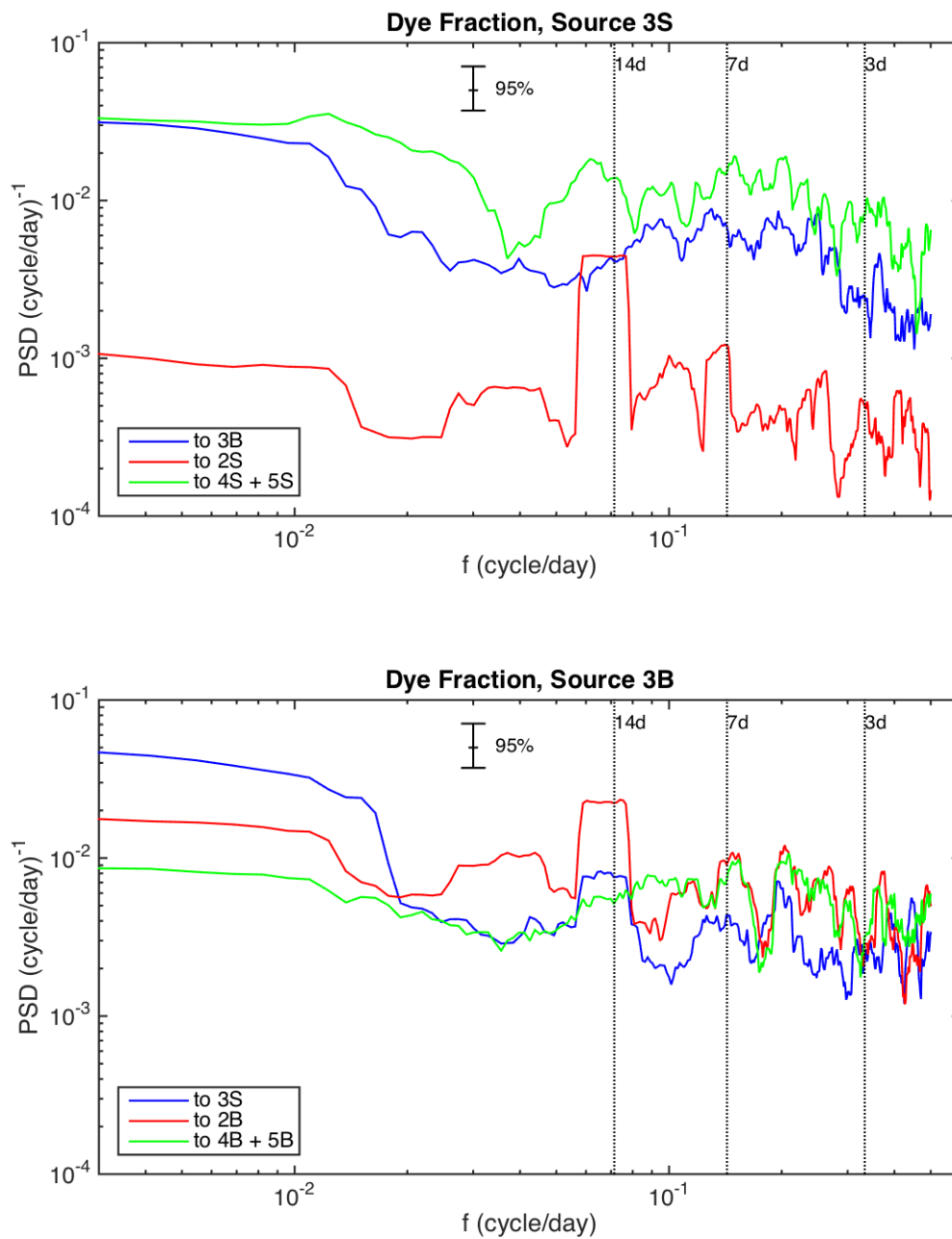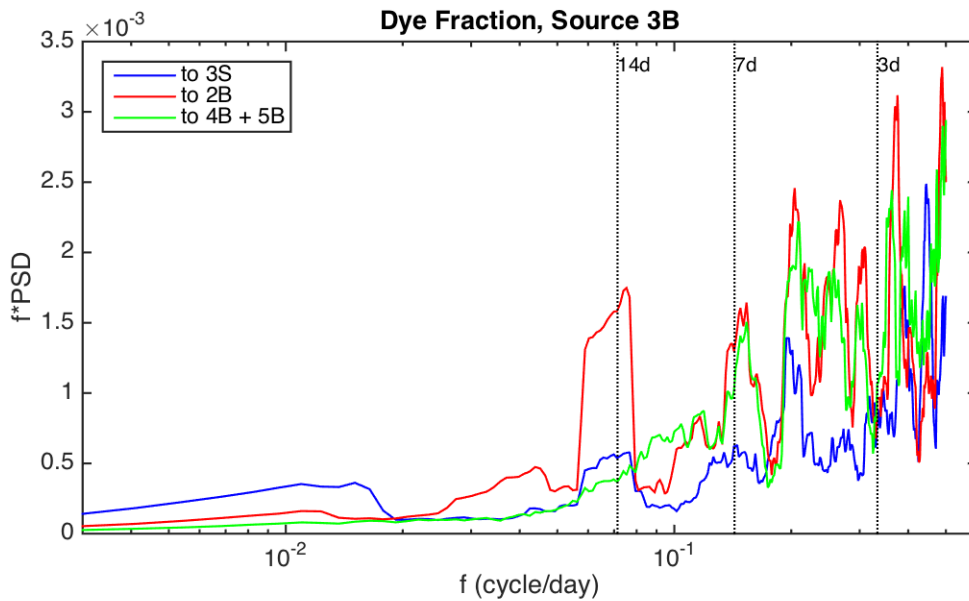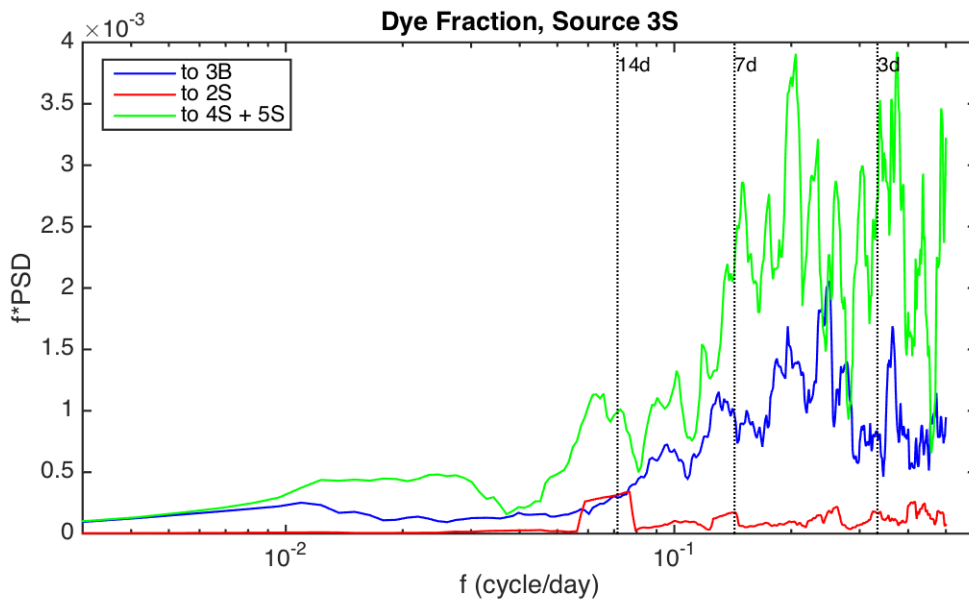ements in EcoGEM box 3 (see Figure 2.1 for the box location). The vertical dotted lines indicate periods of 3, 7, and 14 days.

4 Appendices

4.1 Appendix I: Estimating Greenwich Bay River Inflows

The two main streams entering western Greenwich Bay, the Maskerchugg River (entering Greenwich Cove) and Hardig Brook (entering Apponaug Cove), are not gauged by USGS on a routine basis. However, estimates of Maskerchugg discharge on 22 individual days during the period 1986–2003 were obtained from the USGS and were compared with measured discharge of the nearby Hunt River on the same days. A regression, developed from these data, was used to predict the Maskerchugg discharge from the measured Hunt discharge for each day during the time period of the model run. The resulting regression equation was

$$Q_{Maskerchugg} = c_0 + c_1 Q_{Hunt}, \tag{4.1}$$

where $Q_{Maskerchugg}$ is the estimated Maskerchugg River discharge, Q_{Hunt} is the measured Hunt River discharge, the coefficients are $c_0 = -0.06$ and $c_1 = 0.225$, and the discharges are in units of m^3/s. The root mean square difference between observed and estimated Maskerchugg discharge was 0.06 m^3/s and the correlation coefficient between these two time series was 0.98.

The Hardig Brook discharge was then estimated from the Maskerchugg estimate by assuming that the discharges of these rivers are proportional to their drainage areas: $Q_{Hardig} = Q_{Maskerchugg} * DA_{Hardig}/DA_{Maskerchugg}$ where DA is the river drainage area ($DA_{Maskerchugg} = 15.5$ km^2 and $DA_{Hardig} = 15.8$ km^2).

4.2 Appendix II: Specification of River Water Temperature

River water temperatures are not routinely measured by USGS. However, a 1-year record of river temperature for a single Rhode Island river was obtained from USGS, and these data were used to develop an empirical method to predict river temperature from easily obtained air temperature. The resulting water temperature was applied to all rivers. Temperature of the river water each day was specified as a function of air temperature on that day and the previous day and the water temperature of the previous day. The form of the function was

$$T_{river}^n = a_0 + a_1 T_{river}^{n-1} + a_2 T_{air}^n + a_3 T_{air}^{n-1}, \tag{4.2}$$

where T_{river} and T_{air} are the river and air temperatures and the superscripts *n, n-1* refer to the *n*th day and the prior day respectively. The coefficients in Equation 4.2 were derived using regression techniques with water temperature observations from the Wood River (western RI) over a 1-year period (Oct. 2007-Oct. 2008) and PORTS air temperature data for the same period. Although river temperature exhibits diurnal variability, the fact that the river transport is specified on a daily basis called for the

Coefficient	Value
a_0	0.163
a_1	0.796
a_2	0.187
a_3	0.019

Table 4.1: Regression coefficients for the relationship given by Equation 4.2.

specification of a daily-averaged river temperature value. For this reason, both T_{air} (averaged over all NB PORTS stations) and T_{river} were low-pass filtered (cutoff period = 36 h) to remove diurnal variability and then subsampled to 1 value per day prior to computing the regression. The regression coefficients in Equation 4.2 are given in Table 4.1. Comparing the river temperature predicted using Equation 4.2 with the actual (filtered and subsampled) temperature yielded a correlation coefficient of 0.98 and a root mean square difference of 1.5 °C.

5   Acknowledgements

Bibliography

Balt, C. (2014). *Subestuarine circulation and dispersion in Narragansett Bay.* Ph. D. thesis, Graduate School of Oceanography, University of Rhode Island.

Chapman, D. C. (1985). Numerical treatment of cross-shelf open boundaries in a barotropic coastal ocean model. *Journal of Physical Oceanography 15*, 1060–1075.

Chen, C., R. C. Beardsley, S. Hu, Q. Xu, and H. Lin (2005). Using MM5 to hindcast the ocean surface forcing fields over the Gulf of Maine and Georges Bank region. *Journal of Atmospheric and Oceanic Technology 22*, 131–145.

Codiga, D. L., H. E. Stoffel, C. F. Deacutis, S. Kiernan, and C. A. Oviatt (2009). Narragansett Bay hypoxic event characteristics based on fixed-site monitoring network time series: Intermittency, geographic distribution, spatial synchronicity, and interannual variability. *Estuaries and Coasts 32*, 621–641.

Fairall, C. W., E. F. Bradley, J. E. Hare, A. A. Grachev, and J. Edson (2003). Bulk parameterization of air-sea fluxes: Updates and verification for the COARE algorithm. *Journal of Climate 16*, 571–591.

Flather, R. A. (1976). A tidal model of the northwest European continental shelf. *Memoires de la Societe Royale de Sciences de Liege 6*, 141–164.

Galperin, B., L. H. Kantha, S. Hassid, and A. Rosati (1988). A quasi-equilibrium turbulent energy model for geophysical flows. *Journal of Atmospheric Sciences 45*, 55–62.

Kremer, J. N., J. M. P. Vaudrey, D. S. Ullman, D. L. Bergondo, N. LaSota, C. Kincaid, D. L. Codiga, and M. J. Brush (2010). Simulating property exchange in estuarine ecosystem models at ecologically appropriate scales. *Ecological Modelling 221*, 1080–1088.

Marchesiello, P., J. C. McWilliams, and A. Shchepetkin (2001). Open boundary conditions for long-term integration of regional oceanic models. *Ocean Modelling 3*, 1–20.

Mukai, A. Y., J. J. Westerink, R. A. L. Jr., and D. Mark (2002). Eastcoast 2001: A tidal constituent database for the western North Atlantic, Gulf of Mexico and Caribbean Sea. Technical Report ERDC/CHL TR-02-24, U. S. Army Engineer Research and Development Center, Coastal and Hydraulics Laboratory.

Rogers, J. M. (2008). Circulation and transport in the heart of Narragansett Bay. Master's thesis, Graduate School of Oceanography, University of Rhode Island.

Taylor, K. E. (2001). Summarizing multiple aspects of model performance in a single diagram. *Journal of Geophysical Research 106*, 7183–7192.

Vaudrey, J. M. P. (2016). EcoGEM: Modeling Response of Hypoxia to Changes in Nutrient Inputs to Narragansett Bay, RI, USA. Technical report, Department of Marine Sciences, University of Connecticut. Prepared for NOAA-CHRP.

Warner, J. C., C. R. Sherwood, H. G. Arango, and R. P. Signell (2005). Performance of four turbulence closure models implemented using a generic length scale method. *Ocean Modelling 8*, 81–113.

Willmott, C. J. (1982). Some comments on the evaluation of model performance. *Bulletin of the American Meteorological Society 63*, 1309–1313.